Université d'Ottawa • University of Ottawa

Université d'Ottawa · University of Ottawa

FACULTÉ DES ÉTUDES SUPÉRIEURES ET POSTDOCTORALES

FACULTY OF GRADUATE AND POSTDOCTORAL STUDIES

SOORIYADEVAN, Pradiv

AUTEUR DE LA THÈSE - AUTHOR OF THESIS

M.A.Sc. (Electrical Engineering)

GRADE - DEGREE

School of Information Technology and Engineering)

FACULTÉ, ÉCOLE, DÉPARTEMENT - FACULTY, SCHOOL, DEPARTMENT

TITRE DE LA THÈSE - TITLE OF THE THESIS

The Electromagnetic Modelling and Optimization of Planar Holographic Antennas

Derek McNamara

DIRECTEUR DE LA THÈSE - THESIS SUPERVISOR

EXAMINATEURS DE LA THÈSE - THESIS EXAMINERS

M. Yagoub

A. Petosa

J.-M. De Koninck, Ph.D.

LE DOYEN DE LA FACULTÉ DES ÉTUDES SUPÉRIEURES ET POSTDOCTORALES

SIGNATURE

DEAN OF THE FACULTY OF GRADUATE AND POSTDOCTORAL STUDIES

THE ELECTROMAGNETIC MODELLING AND OPTIMIZATION OF PLANAR HOLOGRAPHIC ANTENNAS

Pradiv Sooriyadevan

Thesis submitted to the
Faculty of Graduate and Postdoctoral Studies
in partial fulfillment of the requirements for the degree of

Master of Applied Science

in

Electrical Engineering

School of Information Technology and Engineering
Ottawa-Carleton Institute for Electrical and Computer Engineering
Faculty of Engineering
University of Ottawa

March, 2004

Your file Votre référence
ISBN: 0-494-01611-6
Our file Notre référence
ISBN: 0-494-01611-6

ABSTRACT

Antennas based on holographic principles are attractive at millimetre wave frequencies because of their potentially relatively high directivity and low profile. Most published design work on planar holographic antennas has been based on approximate expressions and experimental experience. Little attempt appears to have made to use some computational electromagnetics approach to model these antennas. Thus no numerical optimization has been possible.

One aspect that makes the modeling/optimization process difficult is that such planar holographic antennas are electrically large. For instance, in the case of a holographic antenna of directivity 18 dBi, the combined length of the conducting strips on the antennas can be more than $100\lambda_0$. In this thesis we formulate and implement a two-dimensional electromagnetic analysis that allows one to determine the H-plane radiation characteristics of the holographic antenna. This analysis consists of an integral equation formulation for a line source illuminating a structure consisting of conducting strips and dielectric material, plus feedhorn walls, and its solution using the method of moments. We demonstrate how it can be applied in the modeling of the holographic antennas in question. It is possible to model the holographic antenna's feedhorn, the holographic antenna proper, and its interaction with the feedhorn. In addition, we have integrated the electromagnetic analysis with numerical optimization algorithms, and show what antenna geometries (such as the distribution of conducting strip widths) are obtruded by such algorithms as being optimum in some sense. Experimental validation is

provided, and shows that it is possible to improve the gain of the holographic antenna by up to roughly 2 dB.

ACKNOWLEDGEMENTS

I am deeply indebted to my supervisor Prof. Derek McNamara for his guidance and support throughout the thesis. I have enjoyed working with him and the knowledge that I gained from him during this time was invaluable. I would also like to thank him for providing me the resources to carry out this work.

I am grateful to Mr. Michel Cuhaci, Manager of the Advanced Antenna Technology Lab at the Communications Research Center, for providing the materials, fabrication facilities and measurement facilities used for this thesis. I am grateful to Dr. Aldo Petosa, Mr. Soulideth Thirakoune and Dr. Apisak Ittipiboon (of the above group) for their advice, ideas, suggestions and much assistance.

Last but not least, I thank my parents, family members, friends and colleagues for their support.

TABLE OF CONTENTS

LIST OF FIGURES

LIST OF TABLES

GLOSSARY

$\hat{a}(\underline{\rho}')$	Equivalent electric current source on C_h contributing to $\hat{E}_z^s$
$\hat{b}(\underline{\rho}')$	Equivalent electric current source on C_h contributing to $\hat{E}_z^{int}$
B	Back lobe in the far-field radiation pattern (ϕ=-90°)
C_d	Surface along the dielectric
C_h	Surface along the horn
C_s	Surface along the strips
ΔC_j	Length of the j^{th} segment
$D(\phi)$	Two-dimensional directivity at angle ϕ
$\hat{E}_z^{ext}$	Total external electric field, sum of $\hat{E}_z^s$ and $\hat{E}_z^i$
$\hat{E}_z^i$	Electric Field in free-space due to the electric line source
$\hat{E}_z^{int}$	Electric field inside the dielectric
$\hat{E}_z^s$	Scattered electric field in free-space
f	Frequency
$\hat{f}(\underline{\rho}')$	Equivalent electric current source on C_d and C_s contributing to $\hat{E}_z^{int}$
F	Front lobe in the far-field radiation pattern (ϕ=90°)
$\hat{g}(\underline{\rho}')$	Equivalent electric current source on C_d and C_s contributing to $\hat{E}_z^s$
$H_o^{(2)}$	Hankel function of the second kind, zero order
$\underline{\hat{H}}^{ext}$	Total external magnetic field, sum of $\underline{\hat{H}}^s$ and $\underline{\hat{H}}^i$
$\underline{\hat{H}}^i$	Magnetic Field in free-space due to the electric line source
$\underline{\hat{H}}^{int}$	Magnetic field inside the dielectric
$\underline{\hat{H}}^s$	Scattered magnetic field in free-space
$\underline{n}_j$	Unit normal vector to the j^{th} straight line segment
N_d	Number of Segments on the dielectric
N_h	Number of Segments on the horn
N_s	Number of Segments on the strips
P_j	Pulse expansion function of the j^{th} segment
$\underline{R}_{ij}$	Vector from the mid-point of the j^{th} segment to the midpoint of the i^{th} segment
t	Arc length along the straight line segments; or thickness of dielectric slab
$\underline{t}_j$	Unit tangential vector to the jth segment
t_x	x-component of $\underline{t}_j$
t_y	y-component of $\underline{t}_j$
$t_1(j)$	Starting point of the j^{th} segment
$t_2(j)$	End point of the j^{th} segment
T	Lobe away from the feed in the far-field radiation pattern (ϕ=0°)
s	Spacing between successive strip centers

S	Lobe towards feed in the far-field radiation pattern (ϕ=180°)
$S(\phi)$	Power density at the angle ϕ
$U(\phi)$	Radiation intensity at the angle ϕ
$U_{avg.}$	Average radiation intensity
w	Width of the conducting strips
W_i	Weighting function of the i^{th} segment
x	x coordinate of the observation point
$x_c(i)$	x coordinate of the i^{th} segment center point
x_o	x coordinate of the line source
$\underline{u}_x$	unit x vector
$\underline{u}_y$	unit y vector
$\underline{u}_z$	unit z vector
y	y coordinate of the observation point
$y_c(i)$	y coordinate of the i^{th} segment center point
y_o	y coordinate of the line source
β	Phase constant
ε	Permittivity, ($\varepsilon_o\varepsilon_r$) of dielectric in units of [F/m]
ε_o	Permittivity of free-space ($8.854 \cdot 10^{-12}$ [F/m])
ε_r	Relative permittivity of dielectric, also known as relative dielectric constant
λ_o	Free-space wavelength
λ_g	Guide wavelength of the E-fields travelling along the slab
κ	Wave number in dielectric
κ_o	Wave number in free-space
η	Intrinsic impedance of dielectric
η_o	Intrinsic impedance of free-space
ϕ	Observation angle in a anti-clockwise direction from the positive x-axis
$\underline{\rho} = \underline{u}_x x + \underline{u}_y y$	Observation point vector
$\underline{\rho}' = \underline{u}_x x' + \underline{u}_y y'$	Source point vector
μ_o	Permeability of free-space ($4\pi \cdot 10^{-7}$ [H/m])

CHAPTER 1

Introduction

1.1 Background on Holographic Antennas

A planar hologram is a recording, in some sense, of the interference pattern of two wavefronts on a surface. Once such a hologram has been fabricated one of the interfering wavefronts can be recreated by illuminating the hologram with the other interfering wavefront. At optical frequencies the hologram is fabricated by regarding the interference pattern on a photosensitive film. Thus it is possible to record varying levels of constructive and deconstructive interference (i.e. "shades of grey"). At microwave/millimetrewave frequencies fabrication limitations imply that we have to use a binary amplitude approximation of the hologram. This reduces the interference pattern to one consisting of opaque or transparent sections. This hologram is then fabricated using conducting tracks on a dielectric substrate. The presence or absence of a conducting track is used to realize the above mentioned opaque or transparent sections, respectively.

The holographic antenna of interest in this thesis is based on that proposed in [1], but which have more recently been extended and thoroughly studied in [2]. Most published design work on planar holographic antennas has been based on approximate expressions and experimental experience. Little attempt appears to have yet been made to use some computational electromagnetics approach to model these antennas. Thus no numerical optimization has been possible.

One aspect that makes the modeling/optimization process difficult is that such planar holographic antennas are electrically large and materially inhomogeneous. For

instance, in the case of a holographic antenna of directivity 18 dBi, the combined length of the conducting strips on the antennas can be more than $100\lambda_o$.

The holographic antennas have a relatively high gain and low-profile at Ka-Band frequencies. They have much less complexity of design compared to reflector antennas and microwave phased arrays. The feed can be incorporated into the same plane as the slab which makes it easy to fabricate using printed circuit technology, light-weight and inexpensive. It would also not suffer from aperture feed blockage as in reflector antennas. It does not have the complexity and feed losses incurred in passive microwave phased arrays. These reasons make holographic antennas a good candidate for low-cost LMCS and SATCOM terminals.

1.2 Thesis Objectives

In this thesis we formulate and implement a two-dimensional analysis that allows one to determine the H-plane radiation characteristics of the holographic antenna. This analysis consists of an integral equation formulation for a line source illuminating a structure consisting of conducting strips and dielectric material, and its solution using the method of moments. We demonstrate how it can be applied in the modeling of the holographic antennas in question. It is possible to model the holographic antenna's feedhorn, the holographic antenna proper, and its interaction with the feedhorn. In addition, we have integrated the electromagnetic analysis with numerical optimization algorithms, and show what antenna geometries (such as the distribution of conducting strip widths) are obtruded by such algorithms as being optimum in some sense. Experimental validation is provided. The electromagnetic model will also be used to

demonstrate the effect, on antenna performance, for such factors as substrate permittivity and thickness.

1.3 Thesis Organization

Chapter 2 provides a brief review of the planar holographic antenna whose electromagnetic analysis and optimization forms the subject of this thesis.

Chapter 3 presents the theory behind the electromagnetic simulation tool developed and used in the thesis. A set of coupled integral equations that constitutes the 2D electromagnetic model is derived. The moment method formulation for the numerical solution of this electromagnetic model is then provided, along with all the expressions needed for its implementation.

In Chapter 4 the electromagnetic simulation tool is validated in various ways, including through comparison of computed and measured radiation patterns of existing holographic antennas.

Chapter 5 describes how the electromagnetic analysis tool is combined with a numerical optimization algorithm. Optimization (variation of the conducting strip widths and spacings) is then applied to both single-sided and double-sided holographic antennas, and the computed performance of the resulting antennas is compared to measured patterns of associated hardware.

Chapter 6 uses the electromagnetic analysis tool to determine the influence of substrate properties (i.e. relative permittivity and thickness) and the number of conducting strips used on the antenna performance. This allows us to suggest a structured design procedure for such antennas.

Chapter 7 summarizes the contribution of this thesis, draws some general conclusions, and suggests a path that future work on the topic might follow.

1.4 References for Chapter 1

[1] K. Iizuka , M. Mizusawa, S. Urasahi & H. Ushigaone, "Volume-type holographic antenna", *IEEE Transactions on Antennas and Propagation*, vol. AP-23, November 1975, pp. 807-810

[2] K. Lévis, A. Ittipiboon, A. Petosa, L. Roy & P. Berini, "Ka-Band dipole holographic antennas", *IEE Proc.- Microwaves Antennas Propagation*, Vol. 148, No. 2, pp. 129-132, April 2001

CHAPTER 2

The Planar Holographic Antenna

2.1 The Single-Sided Holographic Antenna

The aim of this chapter is to provide a brief review of the geometry and performance of the holographic antenna whose electromagnetic analysis and optimization is the subject of this thesis. The basic principles of a holographic antenna were stated in Section 1.1. In the case of the particular planar holographic antenna in question the interfering wavefronts referred to in Section 1.1 are a spherical wave and a plane wave; the interference pattern is "recorded" in a plane normal to the direction of propagation of the plane wavefront and containing the point from which the spherical wave emanates. The interference pattern (i.e. the hologram) consists of a number of concentric rings [1,2], with complete destructive interference occurring in rings that are a wavelength apart. The approximate binary implementation of the hologram at microwave/millimetrewave frequencies consists of conducting strips etched on a dielectric substrate, as illustrated in Figure 2.1. These strips are located on the rings of complete destructive interference (zero field), and the electric field is tangential to the conducting strips in order for the strips to emulate such rings. Thus the H-plane of the antenna is the x-y plane, and we will label the angle measured away from the x-axis towards the y-axis as ϕ. If a spherical wave from the feed horn illuminates the hologram, the wavefront reconstruction process predicts that we should expect four beams at right angles to each other, two of which correspond to the plane wave used to generate the interference pattern (and which constitute the intended main lobes of the holographic antenna in directions broadside to

the dielectric substrate). This is illustrated in Figure 2.2. Use of the labeling T, B, F and S shown in Figure 2.2 will allow conciseness of expression throughout the thesis.

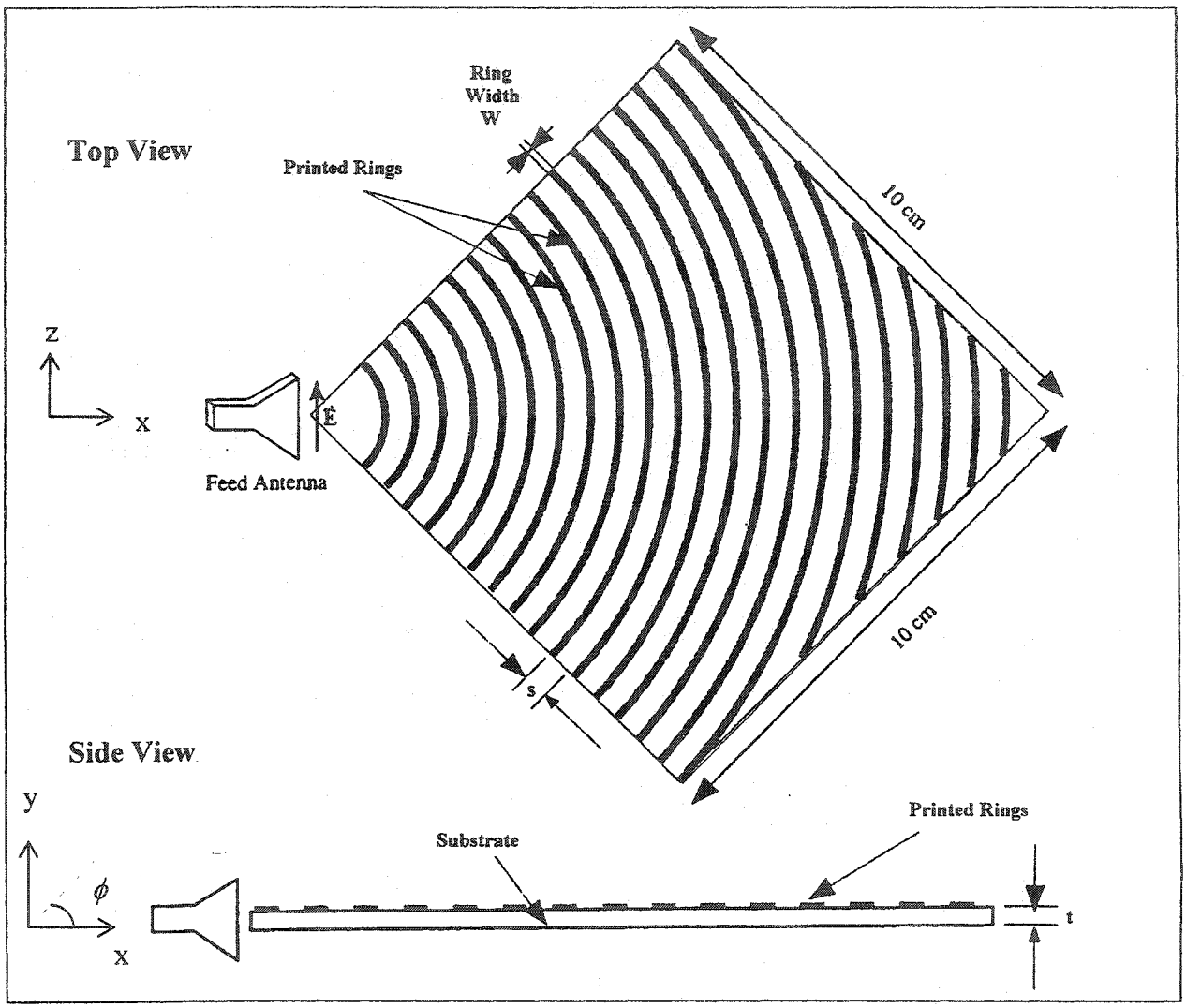

Figure 2.1: Holographic Antenna Geometry [3]

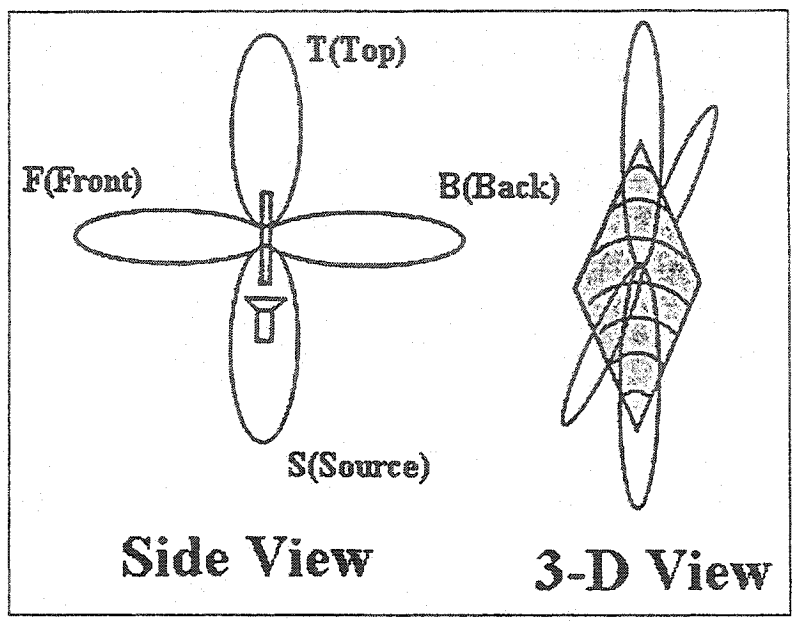

Figure 2.2: Radiation Lobes of the Holographic Antenna (After [2])

As stated in Section 1.1, the above mentioned realization of the interference pattern is approximate. In [1] the conducting strips were made as small as possible in an attempt to approximate the rings of complete destructive interference by lines rather than annuli. Figure 2.3 below shows the measured H-plane radiation pattern of a single-sided holographic antenna. The principle lobes *F* and *B* are clearly visible in Figure 2.3. The *S* lobe (not shown in Figure 2.3) towards the source is blocked by the feed horn and is thus significantly reduced. The *T* lobe is in a direction away from the source. The measured pattern shown in Figure 2.3 was performed using the experimental set-up shown in Appendix E. With the test jig mounted on the test chamber positioner, which is covered with absorber, it is possible to measure radiation patterns out to about ±120°; beyond that the antenna is blocked by the positioner and its absorber. We have therefore restricted the angular region to ±120° whenever showing measured patterns.

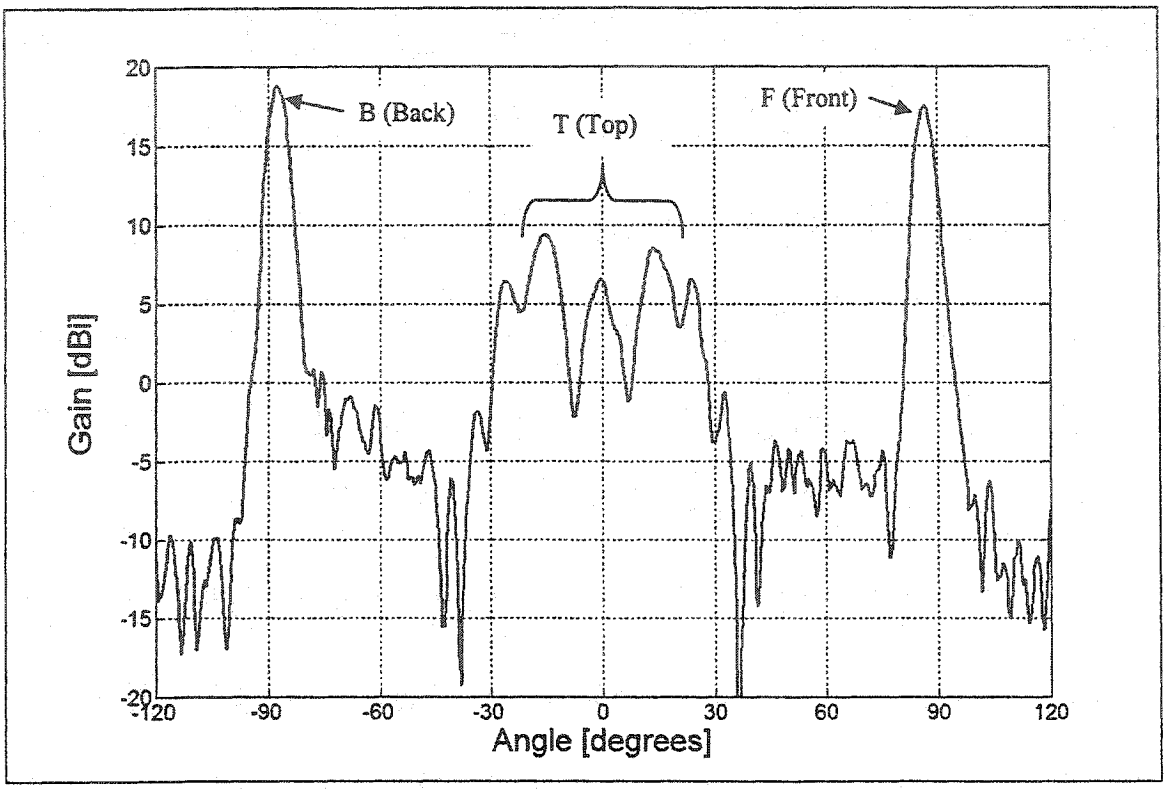

Figure 2.3: Measured H-Plane Radiation Pattern of a Single-Sided Holographic Antenna Versus Angle (ϕ) at 30 GHz.

2.2 The Double-Sided Holographic Antenna

In order to obtain a single dominant lobe (which is required in most general applications) it is necessary to use a double-sided holographic antenna such as that in Figure 2.4. This setup has strips on the bottom of the substrate in addition to those on the top of the substrate. The strips are arranged in such a way that the fields produced by the two sides (top and bottom) cancel each other in the direction of the *B* and S lobes, and add up in the direction of the *F* and *T* lobes. This property can be seen from the measured H-plane field patterns in Figure 2.5. The horizontal shift d_1 between the top and bottom layer of strips, as indicated in Figure 2.4, is $\lambda_o/4$. This corresponds to a 90° phase shift along the slab. The thickness of the slab d_2 in this case is $\lambda_g/4$ also corresponds to a phase

shift of 90° where λ_g is the guide wavelength of the electromagnetic field traveling along the slab.

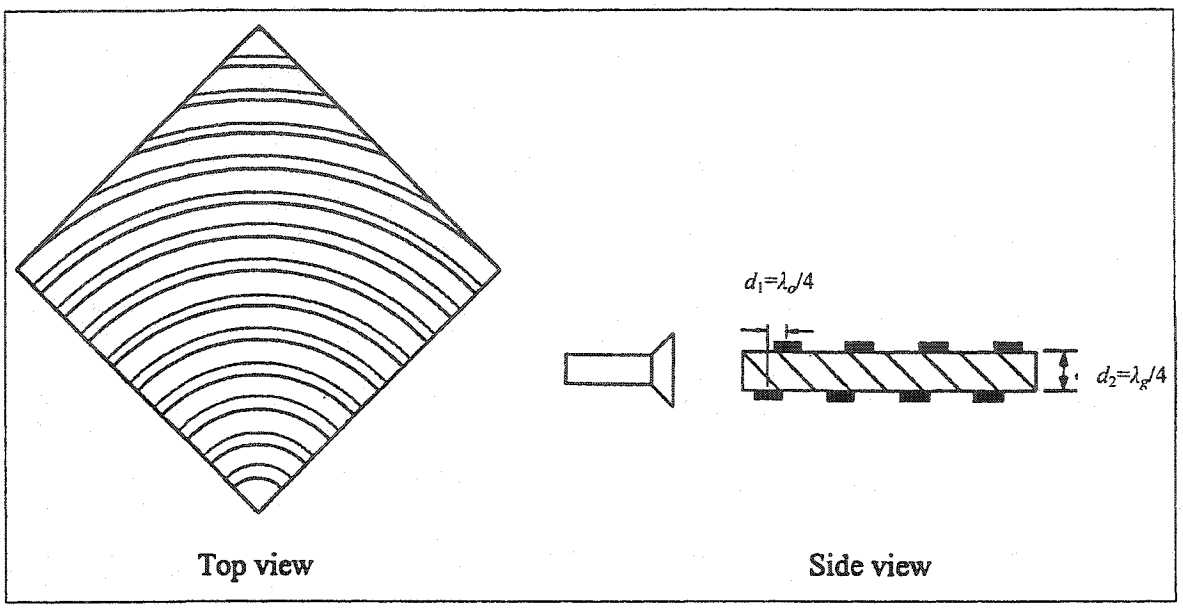

Figure 2.4: Double-Sided Holographic Antenna Geometry [3]

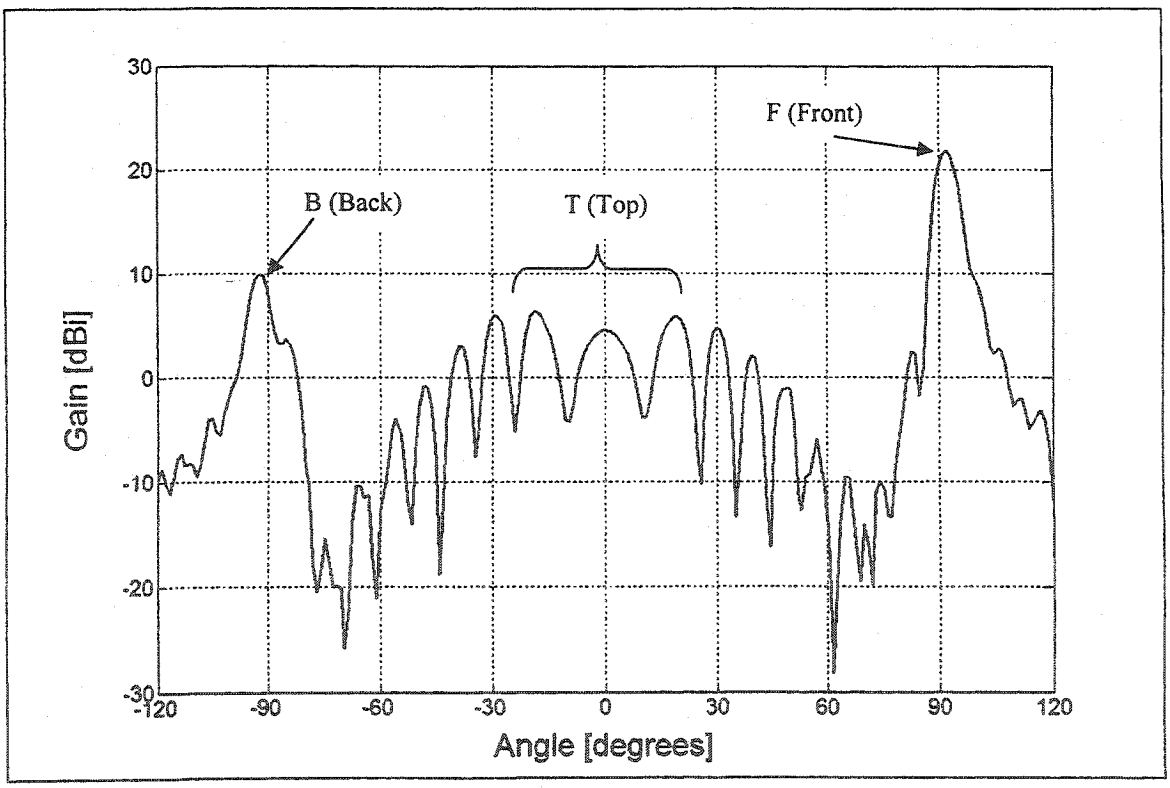

Figure 2.5: Measured H-Plane Radiation Pattern of a Double-Sided Holographic Antenna Versus Angle (ϕ) at 26 GHz.

2.3 References for Chapter 2

[1] K. Lévis, A. Ittipiboon, A. Petosa, L. Roy, and P. Berini, "Ka-Band Dipole Holographic Antennas', IEE Proc.-Microwave Antennas Propagation, Vol. 148, No. 2, pp.129-132, April 2001.

[2] K. Lévis, "Ka-Band Holographic Antennas", Master of Applied Science Thesis, Faculty of Engineering, University of Ottawa, September 1999.

[3] *Private Communication* with A. Petosa, Advanced Antenna Technology Lab, Communications Research Centre, Ottawa, Ontario, Canada.

CHAPTER 3

Electromagnetic Modelling of the Holographic Antenna: Integral Equation-Moment Method Formulation

3.1 Preliminary Remarks

In this chapter, a computational electromagnetics approach is used to model the antenna. A two-dimensional (2D) integral equation formulation is used to model the antenna in its H-plane. Motivation for adopting this approach is presented in Section 3.2. Coupled integral equations are obtained for the 2D equivalent currents that model the structure; this is done using the physical boundary conditions and the surface equivalence theorem. The method of moments with pulse expansion functions and Dirac delta weighting functions (i.e. point matching) is used to solve these integral equations. Expressions for the elements of the moment method impedance and excitation matrix are derived. A FORTRAN code is developed to implement the moment method formulation, and to use the resulting equivalent currents to obtain the near and far-zone electric fields.

3.2 Motivation for Using Two-Dimensional Electromagnetic Models

It is difficult and complicated to simulate a fully 3-dimensional electromagnetic model for the high-directivity holographic antenna under discussion since it is electrically large and dielectrically inhomogeneous. The total length of conducting strip of the antenna in [1], for instance, is more than $100\lambda_o$. The computational burden is simply too large, even with present-day computers, especially if one remembers that we wish to perform optimization of the antennas and that many simulations are required during execution of an optimization algorithm. We therefore use a two-dimensional (2D) model

that allows one to determine the H-plane radiation characteristics of the holographic antenna. Optimization of the antenna using objective functions based on its H-plane radiation patterns will be shown in Chapter 5 to provide antennas with improved performance. A related approach to electromagnetic modeling of the principal plane patterns of horn antennas with complex flare geometries has been described in [2,3].

The 2D model of the holographic antenna is sketched in Figure 3.1, and to this we apply a 2D integral equation formulation, consisting of a line source that illuminates a structure consisting of conducting strips and dielectric material. In this way it is possible to model the holographic antenna's feedhorn, the holographic antenna proper, and its interaction with the feedhorn. The model is validated in Chapters 4 through 5. The integral equation used here, where the dielectric material plays a crucial role in the antenna performance, is more complicated than that used in [2,3], where only conducting materials were present. We have used the integral equation formulation described in [4] as the basis of our formulation, but have extended it so as to be able to accommodate more than just a single dielectric object partially covered by conductors. This extension is described in Section 3.3. The resulting additional moment method matrix and excitation matrix terms are derived in Section 3.4.

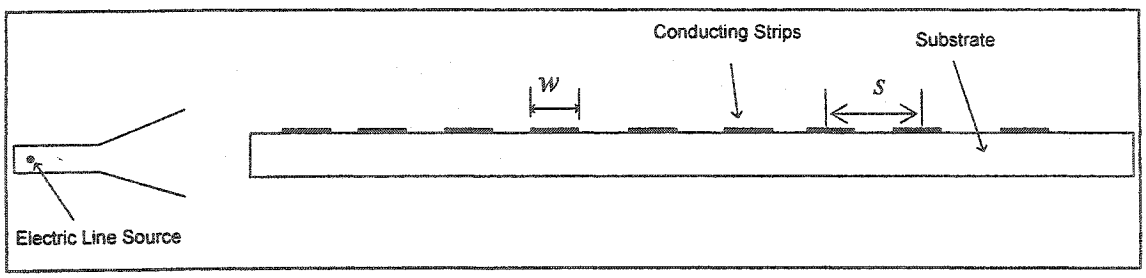

Figure 3.1: Two-Dimensional Cross-Sectional "H-Plane View" of a Single-Sided Holographic Antenna

3.3 Derivation of the Integral Equation

The horn antenna is modelled by an infinitely long electric line source plus conducting walls (this is a TM_z problem). The incident field from this line source (i.e. the impressed field) excites the wall surface of the horn, the dielectric slab and the conducting strips, resulting in scattered fields internal and external to the dielectric. These scattered fields are considered to be produced by equivalent electric currents (an "internal' current density and an "external" current density [4]) on these surfaces. The external field is the sum of the incident field and the scattered field (due to the external equivalent current density) outside the dielectric. The internal total field is due to the internal equivalent current density. Boundary conditions for the continuity of tangential electric and magnetic fields along the dielectric surface, and zero tangential electric fields on the conducting strips and horn walls, are used in obtaining the integral equations. Application of the method of moments results in a matrix equation. Pulse expansion functions and point matching weighting functions are used in the moment method formulation. This matrix equation is solved to obtain the internal and external equivalent currents, from which the electric fields of the antenna can be calculated.

Initially we consider the problem of electromagnetic scattering due to a single dielectric slab and conducting strips, as described in [4]. The solution to this problem is given in [4] for the TM_z case. The horn is ignored for the time being. The scattered field in this case is generated by the conduction currents on the strips and the polarization currents in the dielectric. The surface equivalence theorem is used to formulate the problem in terms of equivalent electric current sources on the dielectric surface C_d and

conducting strips surface C_s. Surfaces C_d and C_s are shown in Figure 3.2. The sides of the dielectric are part of C_d as well.

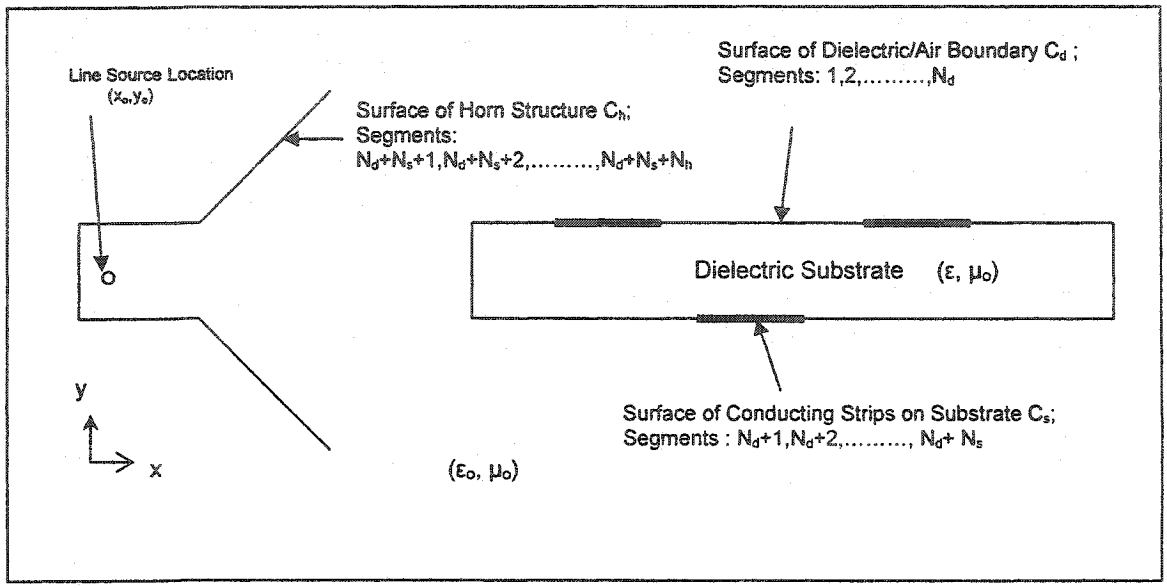

Figure 3.2: Segmentation of the 2D Model of the Holographic Antenna

The electric field internal to the dielectric can be considered to be produced by an equivalent ("internal") electric current density source $\underline{u}_z \hat{f}(\underline{\rho}')$ on C_d and C_s, radiating into the homogenous space filled with dielectric permittivity ε_r everywhere and given by [4]

$$\hat{E}_z^{\text{int}}(\underline{u}_z \hat{f}) = \frac{-\kappa \eta}{4} \int_{C_d+C_s} \hat{f}(\underline{\rho}') H_o^{(2)}(\kappa |\underline{\rho} - \underline{\rho}'|) dt' \qquad (3\text{-}1)$$

where $\kappa = \omega\sqrt{\mu_o \varepsilon}$ is the wave number in the dielectric of permittivity ε, $\eta = \sqrt{\mu_o / \varepsilon}$ is the intrinsic impedance of the dielectric, $\underline{\rho} = \underline{u}_x x + \underline{u}_y y$ is the observation point vector, $\underline{\rho}' = \underline{u}_x x' + \underline{u}_y y'$ is the source point vector, and $H_o^{(2)}$ is the Hankel function of the second kind and zero order. A caret symbol is used on top of all TM_z terms as in [4] to avoid confusion with the TE_z terms of [4] that we will exploit in the extended formulation

described here. Appendix A should be consulted for complete details of the vector coordinate system employed.

The field external to the dielectric can be considered as being the sum of the incident field due to the impressed line source plus a scattered field due to an equivalent ("external") electric current desnsity source $\underline{u}_z \hat{g}(\underline{\rho}')$ on C_d and C_s, and can be written as [4]

$$\hat{E}_z^s(\underline{u}_z \hat{g}) = \frac{-\kappa_o \eta_o}{4} \int_{C_d+C_s} \hat{g}(\underline{\rho}') H_o^{(2)}(\kappa_o |\underline{\rho} - \underline{\rho}'|) dt' \qquad (3\text{-}2)$$

On the dielectric surface the boundary conditions require continuity of the internal and external tangential electric and magnetic fields, as shown below in (3-3) and (3-4) respectively.

$$\hat{E}_z^{\text{int}} = \hat{E}_z^{ext} \qquad \text{over } C_d \qquad (3\text{-}3)$$

$$\underline{n} \times \underline{\hat{H}}^{\text{int}} = \underline{n} \times \underline{\hat{H}}^{ext} \qquad \text{over } C_d \qquad (3\text{-}4)$$

The tangential electric fields must be zero on the strips, as indicated in (3-5).

$$\hat{E}_z^{\text{int}} = \hat{E}_z^{ext} = 0 \qquad \text{over } C_s \qquad (3\text{-}5)$$

Here $\underline{n}$ is a unit vector normal to the relevant boundary. The external electric field $\hat{E}_z^{ext}$ is the sum of the scattered field $\hat{E}_z^s$ due to the equivalent current sources, and the impressed field $\hat{E}_z^i$ due to the line source. This is also true for the external magnetic field $\underline{\hat{H}}^{ext}$. Equations (3-3), (3-4) and (3-5) can thus be rewritten as

$$\underline{u}_z \left(\hat{E}_z^{\text{int}} (\underline{u}_z \hat{f}) - \hat{E}_z^s (\underline{u}_z \hat{g}) \right) = \underline{u}_z \hat{E}_z^i \qquad \textit{over } C_d \qquad (3\text{-}6)$$

$$\underline{n} \times \left(\underline{\hat{H}}^{\text{int}} (\underline{u}_z \hat{f}) - \underline{\hat{H}}^s (\underline{u}_z \hat{g}) \right) = \underline{n} \times \underline{\hat{H}}^i \qquad \textit{over } C_d \qquad (3\text{-}7)$$

$$\underline{u}_z \hat{E}_z^{\text{int}}\left(\underline{u}_z \hat{f}\right) = 0 \qquad \text{over } C_s \qquad (3\text{-}8)$$

$$-\underline{u}_z \hat{E}_z^{s}\left(\underline{u}_z \hat{g}\right) = \underline{u}_z \hat{E}_z^{i} \qquad \text{over } C_s \qquad (3\text{-}9)$$

and represent coupled integral equations for the two sets of unknown equivalent electric currents.

We can extend this formulation to include a second physically separate conducting object needed to model the walls of the horn antenna. When dealing with scatterers that are composed of both conducting and dielectric material this extension is not trivial. Even though the additional object (i.e. the horn walls) is composed of conducting material only, nevertheless two sets of equivalent electric currents must be used to model it in a manner consistent with that used for the dielectric object with the conducting strips. We let $\underline{u}_z \hat{b}(\underline{\rho}')$ and $\underline{u}_z \hat{a}(\underline{\rho}')$ represent the equivalent current density sources on the horn surface C_h; they contribute to both the internal and external fields respectively, namely

$$\hat{E}_z^{\text{int}}(\underline{u}_z \hat{b}) = \frac{-\kappa\,\eta}{4} \int_{C_h} \hat{b}(\underline{\rho}') H_o^{(2)}(\kappa \left| \underline{\rho} - \underline{\rho}' \right|) dt' \qquad (3\text{-}10)$$

$$\hat{E}_z^{s}(\underline{u}_z \hat{a}) = \frac{-\kappa_o \eta_o}{4} \int_{C_h} \hat{a}(\underline{\rho}') H_o^{(2)}(\kappa_o \left| \underline{\rho} - \underline{\rho}' \right|) dt' \qquad (3\text{-}11)$$

Application of the boundary conditions on all conducting surfaces and dielectric interfaces then yields the coupled integral equations of the extended formulation as

$$\underline{u}_z \left(\hat{E}_z^{\text{int}}\left(\underline{u}_z \hat{f}\right) - \hat{E}_z^{s}\left(\underline{u}_z \hat{g}\right) - \hat{E}_z^{s}\left(\underline{u}_z \hat{a}\right) + \hat{E}_z^{\text{int}}\left(\underline{u}_z \hat{b}\right) \right) = \underline{u}_z \hat{E}_z^{i} \qquad \text{over } C_d \qquad (3\text{-}12)$$

$$\underline{n} \times \left(\underline{\hat{H}}^{\text{int}}\left(\underline{u}_z \hat{f}\right) - \underline{\hat{H}}^{s}\left(\underline{u}_z \hat{g}\right) - \underline{\hat{H}}^{s}\left(\underline{u}_z \hat{a}\right) + \underline{\hat{H}}^{\text{int}}\left(\underline{u}_z \hat{b}\right) \right) = \underline{n} \times \underline{\hat{H}}^{i} \qquad \text{over } C_d \qquad (3\text{-}13)$$

$$\underline{u}_z \left(\hat{E}_z^{\text{int}}\left(\underline{u}_z \hat{f}\right) + \hat{E}_z^{\text{int}}\left(\underline{u}_z \hat{b}\right) \right) = 0 \qquad \text{over } C_s \,\&\, C_h \qquad (3\text{-}14)$$

$$-\underline{u}_z\left(\hat{E}_z^s(\underline{u}_z\hat{g})+\hat{E}_z^s(\underline{u}_z\hat{a})\right)=\underline{u}_z E_z^i \qquad \text{over } C_s \text{ \& } C_h \quad (3\text{-}15)$$

3.4 Formulation of the Moment Method Solution of the Extended Integral Equation Formulation

Pulse expansion functions are applied to the above coupled integral equations by dividing the surfaces C_d, C_s and C_h into N_d, N_s and N_h straight-line segments respectively, as shown in Figure 3.2, and approximating the currents as constant over each segment. There are segments along the sides of the dielectric as well which are included in N_d. The equivalent currents thus take the forms

$$\hat{f} = \sum_{j=1}^{N_d+N_s} \hat{f}_j P_j \qquad (3\text{-}16)$$

$$\hat{g} = \sum_{j=1}^{N_d+N_s} \hat{g}_j P_j \qquad (3\text{-}17)$$

$$\hat{b} = \sum_{j=1}^{N_h} \hat{b}_j P_{j+N_d+N_s} \qquad (3\text{-}18)$$

$$\hat{a} = \sum_{j=1}^{N_h} \hat{a}_j P_{j+N_d+N_s} \qquad (3\text{-}19)$$

where

$$P_j = \begin{cases} 1 & t_1(j) \le t \le t_2(j) \\ 0 & elsewhere \end{cases} \qquad (3\text{-}20)$$

P_j is a pulse expansion function with a value of 1 over the j^{th} segment. Quantities $t_1(j)$ and $t_2(j)$ are the starting and end points of the segment, and t is the arc length along the straight line segments, as illustrated in Figure A-1 in Appendix A. Substituting (3-16)

through (3-19) into (3-12) through (3-15), and multiplying both sides of (3-13) by η_o, yields the following intermediate expressions.

$$\sum_{j=1}^{N_d+N_s} \underline{u}_z \hat{f}_j \hat{E}_z^{\text{int}}(\underline{u}_z P_j) + \sum_{j=1}^{N_d+N_s} \underline{u}_z(-\hat{g}_j)\hat{E}_z^s(\underline{u}_z P_j) + \sum_{j=1}^{N_h} \underline{u}_z(-\hat{a}_j)\hat{E}_z^s(\underline{u}_z P_{j+N_d+N_s}) + \sum_{j=1}^{N_h} \underline{u}_z \hat{b}_j \hat{E}_z^{\text{int}}(\underline{u}_z P_{j+N_d+N_s})$$
$$= \underline{u}_z \hat{E}_z^i$$

over C_d (3-21)

$$\eta_o \sum_{j=1}^{N_d+N_s} \hat{f}_j \underline{n}\times\underline{\hat{H}}^{\text{int}}(\underline{u}_z P_j) + \eta_o \sum_{j=1}^{N_d+N_s} (-\hat{g}_j)\underline{n}\times\underline{\hat{H}}^s(\underline{u}_z P_j) + \eta_o \sum_{j=1}^{N_h} (-\hat{a}_j)\underline{n}\times\underline{\hat{H}}^s(\underline{u}_z P_{j+N_d+N_s}) + \eta_o \sum_{j=1}^{N_h} \hat{b}_j \underline{n}\times\underline{\hat{H}}^{\text{int}}(\underline{u}_z P_{j+N_d+N_s})$$
$$= \eta_o \underline{n}\times\underline{\hat{H}}^i$$

over C_d (3-22)

$$\sum_{j=1}^{N_d+N_s} \underline{u}_z \hat{f}_j \hat{E}_z^{\text{int}}(\underline{u}_z P_j) + \sum_{j=1}^{N_h} \underline{u}_z \hat{b}_j \hat{E}_z^{\text{int}}(\underline{u}_z P_{j+N_d+N_s}) = 0$$ over C_s and C_h (3-23)

$$\sum_{j=1}^{N_d+N_s} \underline{u}_z(-\hat{g}_j)\hat{E}_z^s(\underline{u}_z P_j) + \sum_{j=1}^{N_h} \underline{u}_z(-\hat{a}_j)\hat{E}_z^s(\underline{u}_z P_{j+N_d+N_s}) = \underline{u}_z \hat{E}_z^i$$

over C_s and C_h (3-24)

The symmetric product of two vectors $\underline{A}$ and $\underline{B}$ on C is defined as

$$\langle \underline{A}, \underline{B} \rangle = \int_C \underline{A} \bullet \underline{B} \quad dt \tag{3-25}$$

Taking the symmetric product of (3-21) through (3-24) with a set of weighting functions $\underline{u}_z W_i$, we reduce the integral equations (3-12) through (3-15) to the matrix equation

$$\begin{bmatrix} [\hat{Z}_1^{\text{int}}] & [\hat{Z}_1^s] & [\hat{Z}_1^a] & [\hat{Z}_1^b] \\ [\hat{Y}^{\text{int}}] & [\hat{Y}^s] & [\hat{Y}^a] & [\hat{Y}^b] \\ [\hat{Z}_2^{\text{int}}] & [0] & [0] & [\hat{Z}_2^b] \\ [0] & [\hat{Z}_2^s] & [\hat{Z}_2^a] & [0] \end{bmatrix} \begin{bmatrix} [\hat{I}^f] \\ [-\hat{I}^g] \\ [-\hat{I}^a] \\ [\hat{I}^b] \end{bmatrix} = \begin{bmatrix} [\hat{V}_1] \\ [\hat{I}] \\ [0] \\ [\hat{V}_2] \end{bmatrix} \tag{3-26}$$

The j^{th} element of the column vectors $[I_f]$, $[-I_g]$, $[-I_a]$ and $[I_b]$ on (3-26) are the unknown currents f_j, $-g_j$, $-a_j$ and b_j respectively, and are found by solving the above matrix equation. The excitation vector on the right hand side of the equation consists of elements due to the incident electric and magnetic fields from the electric line source. We can write

$$\left[\hat{V}\right] = \begin{bmatrix} \left[\hat{V}_1\right] \\ \left[\hat{V}_2\right] \end{bmatrix} \tag{3-27}$$

where $\left[\hat{V}_1\right]$ and $\left[\hat{V}_2\right]$ are column vectors of size N_d and N_s+N_h respectively. The elements of $\left[\hat{V}\right]$ are found from (3-21) and (3-24) to be

$$\hat{V}_i = \left\langle \underline{u}_z W_i, \underline{u}_z \hat{E}_z^i \right\rangle \tag{3-28}$$

The weighting function W_i is chosen to be the Dirac delta-function $\delta\left(t - \frac{t_1(i)+t_2(i)}{2}\right)$ which is zero everywhere except at the center of the i^{th} segment. The subscript i of the function $u_z W_i$ runs from i=1 to i=N_d over the dielectric surface for (3-21) and (3-22), whereas for (3-23) and (3-24) the i values run from N_d+1 to N_d+N_s+N_h over the horn and strips. Substituting the expression for $\hat{E}_z^i$ from (B-1) of Appendix B, and W_i into (3-28), we obtain

$$\hat{V}_i = -\frac{\kappa_o^2}{4\omega\varepsilon_o} H_0^{(2)}\left(\kappa_o \sqrt{\left(x_c(i)-x_o\right)^2 + \left(y_c(i)-y_o\right)^2}\right) \tag{3-29}$$

where $(x_c(i),y_c(i))$ are the center points of the i^{th} segment (as defined in Appendix A) and (x_o,y_o) are the coordinates of the line source. Column vector $[\hat{I}]$ is a vector of length N_d and is expressed as

$$\hat{I}_i = \eta_o \left\langle \underline{u}_z W_i, \underline{n} \times \underline{\hat{H}}^i \right\rangle \tag{3-30}$$

Performing the vector cross multiplication of the magnetic field $\underline{\hat{H}}^i$ due to the line source, which is derived in (B-6) and (B-7) of Appendix B, with the normal $\underline{n}$ of the i^{th} segment defined in (A-3) in Appendix A, allows us to write

$$\hat{I}_i = \eta_o \left(-t_y \hat{H}_y^i(x_c(i), y_c(i)) - t_x \hat{H}_x^i(x_c(i), y_c(i)) \right) \tag{3-31a}$$

with

$$\hat{H}_x^i(x_c(i), y_c(i)) = -\frac{\kappa_o^2}{4j}(y_c(i) - y_o) \frac{H_1^{(2)}\left\{\kappa_o \sqrt{(x_c(i)-x_o)^2 + (y_c(i)-y_o)^2}\right\}}{k_o \sqrt{(x_c(i)-x_o)^2 + (y_c(i)-y_o)^2}} \tag{3-31b}$$

$$\hat{H}_y^i(x_c(i), y_c(i)) = \frac{\kappa_o^2}{4j}(x_c(i) - x_o) \frac{H_1^{(2)}\left\{\kappa_o \sqrt{(x_c(i)-x_o)^2 + (y_c(i)-y_o)^2}\right\}}{k_o \sqrt{(x_c(i)-x_o)^2 + (y_c(i)-y_o)^2}} \tag{3-31c}$$

Quantities t_x and t_y are the x and y components, respectively, of the unit vector $\underline{t}_i$ along the i^{th} segment, which is derived in (A-1) in Appendix A.

Comparison of (3-21) through (3-24) with matrix equation (3-26) reveals that some of the sub-matrices of the impedance matrix can be grouped together as indicated below in (3-32a), (3-33a), (3-34a) and (3-35a). This is due to the fact that their elements have the same expressions as given in (3-32b), (3-33b), (3-34b) and (3-35b), respectively.

$$\left[\hat{Z}^{\text{int}}\right] = \begin{bmatrix} \left[\hat{Z}_1^{\text{int}}\right] & \left[\hat{Z}_1^{b}\right] \\ \left[\hat{Z}_2^{\text{int}}\right] & \left[\hat{Z}_2^{b}\right] \end{bmatrix} \tag{3-32a}$$

$$\hat{Z}_{ij}^{\text{int}} = \left\langle \underline{u}_z W_i, \underline{u}_z \hat{E}_z^{\text{int}}\left(\underline{u}_z P_j\right) \right\rangle \tag{3-32b}$$

$$[\hat{Z}^s]=\begin{bmatrix}[\hat{Z}_1^s] & [\hat{Z}_1^a]\\ [\hat{Z}_2^s] & [\hat{Z}_2^a]\end{bmatrix} \tag{3-33a}$$

$$\hat{Z}_{ij}^s=\left\langle \underline{u}_z W_i, \underline{u}_z \hat{E}_z^s\left(\underline{u}_z P_j\right)\right\rangle \tag{3-33b}$$

$$[\hat{Y}^{\text{int}}]=[[\hat{Y}^{\text{int}}]\ \ [\hat{Y}^b]] \tag{3-34a}$$

$$\hat{Y}_{ij}^{\text{int}}=\eta_o\left\langle \underline{u}_z W_i, \underline{n}\times \underline{\hat{H}}^{\text{int}}\left(\underline{u}_z P_j\right)\right\rangle \tag{3-34b}$$

$$[\hat{Y}^s]=[[\hat{Y}^s]\ \ [\hat{Y}^a]] \tag{3-35a}$$

$$\hat{Y}_{ij}^s=\eta_o\left\langle \underline{u}_z W_i, \underline{n}\times \underline{\hat{H}}^s\left(\underline{u}_z P_j\right)\right\rangle \tag{3-35b}$$

In [4] the concept of duality was used to obtain the final implementable forms for (3-32b), (3-33b), (3-34b) and (3-35b) from their Transverse-Electric (TE_z) counterpart terms Z_{ij}^{int}, Z_{ij}^s, Y_{ij}^{int} and Y_{ij}^s respectively. The TE_z terms were derived [4]. We can similarly exploit duality, and the mathematical similarity between the expressions for the matrix terms of our extended formulation with various expressions provided in the restricted formulation of [4], to arrive at implementable expressions for the impedance and excitation matrices of the extended formulation. The final implementable expressions for (3-34b) is given by

$$\hat{Y}_{ij}^{\text{int}}=-\eta_o Z_{ij}^{\text{int}} \tag{3-36a}$$

where

$$Z_{ij}^{\text{int}}=\frac{-\kappa\Delta C_j}{8j}\int_{-1}^{1}\left[-\underline{t}_i\cdot\underline{u}_y a_x+\underline{t}_i\cdot\underline{u}_x a_y\right]\frac{H_1^{(2)}\left(\kappa\left|\underline{r}_{ij}\right|\right)}{\left|\underline{r}_{ij}\right|}du' \tag{3-36b}$$

The vector terms $\underline{r}_{ij}$, a_x and a_y, as well as ΔC_j and u', are defined in Appendix A.

Likewise for (3-35b), we obtain

$$\hat{Y}_{ij}^{s} = -\eta_o Z_{ij}^{s} \tag{3-37a}$$

with

$$Z_{ij}^{s} = \frac{-\kappa_o \Delta C_j}{8j} \int_{-1}^{1} \left[-\underline{t}_i \cdot \underline{u}_y a_x + \underline{t}_i \cdot \underline{u}_x a_y \right] \frac{H_1^{(2)}\left(\kappa_o \left|\underline{r}_{ij}\right|\right)}{\left|\underline{r}_{ij}\right|} du' \tag{3-37b}$$

As in [4], the self-terms are evaluated to be

$$Z_{ii}^{\text{int}} = -Z_{ii}^{s} = 1/2 \tag{3-38}$$

For (3-32b) we can write

$$\hat{Z}_{ij}^{\text{int}} = \frac{\eta^2}{\eta_o} Y_{ij}^{\text{int}} \tag{3-39a}$$

with

$$Y_{ij}^{\text{int}} = \frac{-\kappa_o \Delta C_j \varepsilon_r}{8} \int_{-1}^{1} H_0^{(2)}\left(\kappa \left|\underline{r}_{ij}\right|\right) du' \tag{3-39b}$$

and

$$Y_{ii}^{\text{int}} = -\frac{\varepsilon_r \kappa_o \Delta C_i}{4} \left[1 - j\frac{2}{\pi} \left(\log \frac{\gamma \kappa \Delta C_i}{4} - 1 \right) \right] \tag{3-39c}$$

The constant γ=1.781, with $ln(\gamma)$ being Euler's constant. Finally for (3-33b) we have

$$\hat{Z}_{ij}^{s} = \eta_o Y_{ij}^{s} \tag{3-40a}$$

with

$$Y_{ij}^{s} = \frac{-\kappa_o \Delta C_j}{8} \int_{-1}^{1} H_0^{(2)}\left(\kappa_o \left|\underline{r}_{ij}\right|\right) du' \tag{3-40b}$$

and

$$Y_{ii}^{s} = -\frac{\kappa_o \Delta C_i}{4}\left[1 - j\frac{2}{\pi}\left(\log\frac{\gamma\kappa_o \Delta C_i}{4} - 1\right)\right] \qquad (3\text{-}40c)$$

The Hankel function approximation (3-41) given below was used to obtain the self terms (3-39c) and (3-40c), for which $i=j$.

$$H_0^{(2)}(x) \xrightarrow[x\to 0]{} 1 - j\frac{2}{\pi}\log\left(\frac{\gamma x}{2}\right) \qquad (3\text{-}41)$$

3.5 Expression for Near- and Far-Zone Electric Fields in the H-plane

Equations (3-27) to (3-40) can be used to construct the impedance and excitation matrices of equation (3-26). A FORTRAN code is used to evaluate these using the implementable expressions provided in the previous sections. This matrix equation is then solved to obtain the equivalent currents f_j, g_j, a_j and b_j. The external field can then be found by adding the scattered fields produced by equivalent currents g_j and a_j to the field incident from the line source, namely

$$\hat{E}_z^{ext} = \hat{E}_z^{i} + \sum_{j=1}^{N_d+N_s} \underline{u}_z g_j \hat{E}_z^{s}\left(\underline{u}_z P_j\right) + \sum_{j=1}^{N_h} \underline{u}_z a_j \hat{E}_z^{s}\left(\underline{u}_z P_{j+N_d+N_s}\right) \qquad (3\text{-}42)$$

$\hat{E}_z^{i}$ is simply (B1) of Appendix B. The far-zone form of $\hat{E}_z^{ext}$ is used in the 2D directivity expression (C-6) of Appendix C to determine the 2D directivity of the holographic antenna being modelled.

3.6 Summary

In this chapter all expressions necessary to implement a moment method solution of the 2D integral equation model of the holographic antenna have been provided. This is a new integral equation formulation. Whereas the one in [4] permits only a single

conductor/dielectric object, that derived here allows more than one such object to be present. We have also altered the formulation of [4], which considers only excitation by a plane wave, to permit excitation by an electric line source.

The horn antenna is modelled by an infinitely long electric line source plus conducting walls (this is a TM_z problem). The incident field from this line source (i.e. the impressed field) excites the wall surface of the horn, the dielectric slab and the conducting strips, resulting in scattered fields internal and external to the dielectric. These scattered fields are considered to be produced by equivalent electric currents on these surfaces. The external field is the sum of the incident and the scattered field outside the dielectric. Enforcement of the boundary conditions for the continuity of tangential electric and magnetic fields along the dielectric surface, and zero tangential electric fields on the conducting strips and horn walls, yields the set of coupled integral equations. Application of the method of moments to these integral equations reduces them to a matrix equation. Pulse expansion functions and point matching weighting functions are used in the moment method formulation. This matrix equation is solved to obtain the equivalent currents, from which the electric fields of the antenna can be calculated.

There are three parts to the FORTRAN codes written. The first one deals with segmentation of the 2-D surface of the horn walls, the dielectric and the conducting strips when all the dimensions are provided. The second code reads these segment coordinates and builds the impedance and excitation matrices of the matrix equation (3-26) using the expressions derived in Section 3.4, and thereafter solves (3-26) for the unknown equivalent currents. The third code calculates the E-fields due to these currents. These E-

fields are used to find the 2D directivity of the antenna. Near fields can also be calculated using this third code.

At this stage of the work we therefore have a computationally efficient electromagnetic simulation tool that is feasible for use with numerical optimization. However, before proceeding to the application of such optimization in Chapter 5, we will in the next chapter (i.e. Chapter 4) first consider evidence for the validity of the tool as a means of modelling holographic antennas.

3.7 References for Chapter 3

[1] K. Lévis, A. Ittipiboon, A. Petosa, L. Roy, and P. Berini, "Ka-Band Dipole Holographic Antennas', IEE Proc.-Microwave Antennas Propagation, Vol. 148, No. 2, pp.129-132, April 2001.

[2] L. Botha and D.A. McNamara, "Examination of antenna patterns of profiled horns using the method of moments", 1985 IEEE International Antennas and Propagation Symposium Digest (IEEE Catalogue No. 85CH2128-7), Vol.I, pp.293 - 296, Vancouver, Canada.

[3] D.J. Heedy & W.D. Burnside, "An aperture-matched compact range feed horn design", IEEE Trans. Antennas & Propagation, *Vol.*AP-33, pp.1249-1255, 1985.

[4] X. Yuan, R.F. Harrington and S.S. Lee, "Electromagnetic Scattering by a Dielectric Cylinder Partially Covered by Conductors", Journal of Electromagnetic Waves and Applications, Vol. 2, No. 1 21-44, 1987

CHAPTER 4

Implementation, Interpretation & Experimental Validation of the Electromagnetic Modelling Tool

4.1 Introduction

There are two objectives in this chapter. Firstly, we wish to demonstrate that the extended integral equation formulation of Chapter 3, the associated moment method formulation, and the associated code are correct, irrespective of how well it models the holographic antenna in question. Secondly, we wish to demonstrate that the two-dimensional coupled integral equation model constitutes a useful electromagnetic model for the H-plane characteristics of the holographic antenna. In order to achieve this we will make use of two existing pieces of information.

A moment method code based on the integral equation analysis of two-dimensional conducting objects (but no dielectric materials present), which we will refer to as the reference code [1,2], was available for comparison. If we model some geometry with the code developed in this thesis (which we will simply refer to as the thesis code), whose complexity exceeds that of the reference code in that it is able to account for the presence of dielectric materials, then if we set the dielectric relative permittivity in the model to unity we should obtain results identical to that of the reference code. This will be shown to be the case in Section 4.3.

In order to determine whether the extended integral equation formulation is able to reliably model the H-plane patterns of the holographic antenna we will compare computed results to measurements on existing holographic antennas [3,4]. This is the subject of Section 4.4.

The dimensions and other parameters of the two existing holographic antennas (a single-sided antenna and a double-sided one) are provided in Appendix D. We will in the thesis refer to these as the "original" holographic antennas. We will use these dimensions in both Sections 4.3 and 4.4. They will also be used as the starting point when we apply optimization to the antennas in Chapter 5.

4.2 Electromagnetic Model Geometries Used in this Chapter

The dimensions of the two-dimensional model of the original single-sided holographic antenna used in this chapter are shown Figure 4.1. The dimensions of the horn antenna walls are those of the x-y plane projection of the sectoral horn antenna in Figure E.1 of Appendix E. This is used since it is the same horn that will be used in measurements on the optimized antennas in Chapter 5. The excitation of the horn is modelled by using a waveguide section with a line source placed approximately $\lambda_o/4$ (or 2.5 mm for an operating frequency of 30 GHz) away from the short-circuit forming the back wall of the horn. The single-sided holographic antenna is designed for a centre-frequency of 30 GHz, and so the spacing between the strip centers, which according to the discussion of Chapter 2 must be λ_o, is 10 mm in this case. The distance between the dielectric slab and the aperture of the horn is zero; in other words the tip of the holographic antenna is at the horn aperture. The location of the feed horn aperture for this original single-sided holographic antenna was experimentally optimized in [4,pp.58] to provide the best performance. The strips in the original antenna had widths of 10 mils (0.254 mm), this having been used since it was the smallest possible value that could be fabricated. The dielectric slab selected had a thickness 20 mils and a relative dielectric

constant of 3.38. The dimensions of this original single-sided antenna are summarised in Tables D-1 and D-2 of Appendix D.

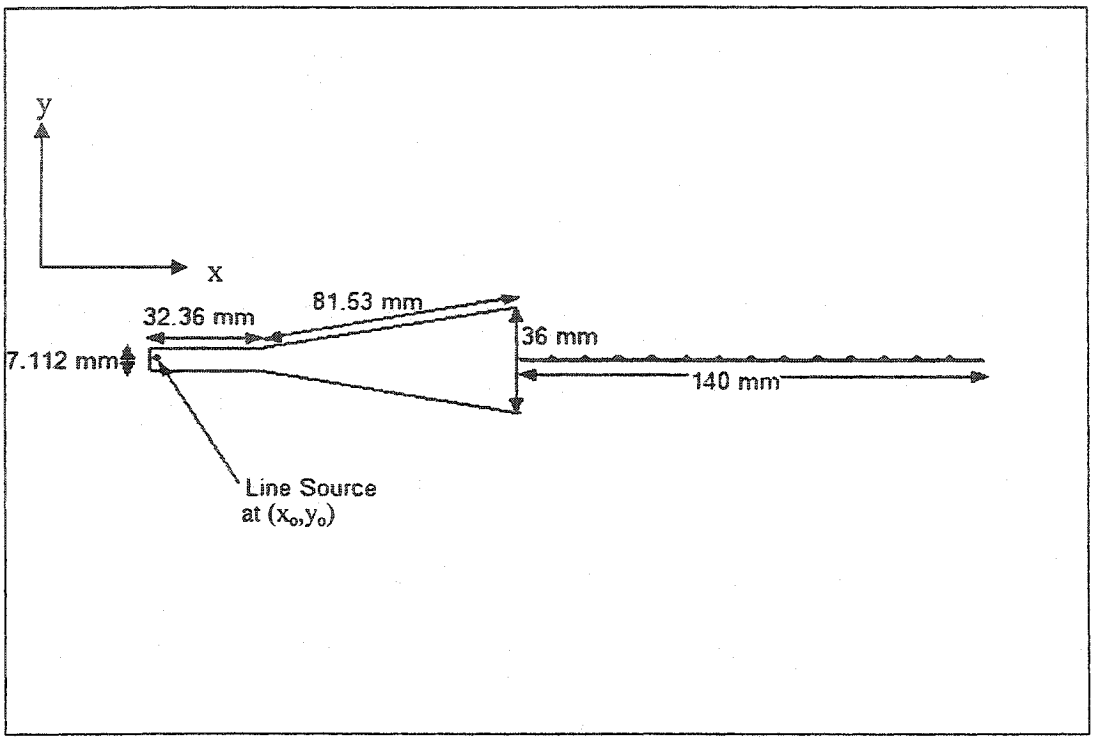

Figure 4.1: Dimensions of the Two-Dimensional Model of the Original Single-Sided Holographic Antenna

As mentioned in Chapter 2, the double-sided holographic antenna has additional strips on the bottom side of the dielectric substrate. The dimensions of the original double-sided holographic antenna are summarised in Tables D.4 and D.5 of Appendix D. It has the same strips widths, and spacing between strips, as the single-sided holographic antenna. However, the strips on the bottom side are shifted with respect to those on the top side by approximately $\lambda_o/4$ (which is 2.5 mm for 30 GHz operation). The substrate (whose ε_r was 3.00) had a thickness of 60 mils, which corresponds to approximately $\lambda_o/4\sqrt{\varepsilon_r}$ at 30 GHz.

This is an appropriate place to briefly discuss what we will mean when comparing computed and measured radiation patterns. In the case of the two-dimensional model it is not possible to determine the true (three-dimensional) directivity; instead we calculate the two-dimensional directivity defined in Appendix C. In Chapter 5, when performing numerical optimization on the holographic antennas, we will optimize the two-dimensional directivity. The argument is that if we optimize this two-dimensional directivity associated with the H-plane of the antenna, we will at once be optimizing the true directivity of the antenna. This will be shown in Chapter 5 to indeed be the case. We note that it is possible to compare computed two-dimensional beamwidths and measured H-plane beamwidths directly.

4.3 Validation of the Integral Equation Formulation & Moment Method Implementation

As stated above, we in this section simply wish to establish the correctness of the formulation presented in Chapter 3, and its subsequent numerical implementation. The computed H-plane pattern for the single-sided holographic antenna, with and without the dielectric present, is shown in Figure 4.2. These were computed using the thesis code. We observed that the pattern without the dielectric present (that is, with ε_r set equal to unity) is absolutely identical to that obtained from the reference code, which is also shown in the same figure. Figure 4.3 shows the effect of slightly increasing the value of ε_r from unity; there is an accompanying gradual change in the computed pattern characteristics as expected. The above computations clearly show the crucial role played by the substrate material, especially as regards to the level of the T lobe. Indeed, even for a very thin substrate case (not used in any of the antennas discussed in this thesis, but used here for

illustration only) shown in Figure 4.4 the effect of the substrate on the radiation pattern, namely the F, B and T lobes, is significant. It is possible to use the electromagnetic simulation tool developed in the thesis to conveniently examine the effects of substrate thickness and permittivity. This will be further illustrated in Chapter 6, where a design procedure for planar holographic antennas is suggested.

We next examine the computed results for the geometry in Fig.4.1, but with the dielectric substrate and strips (i.e. the holographic antenna proper) removed, leaving only the electric line-source and horn walls. The computed H-plane pattern is then that for a horn antenna only, and is shown in Figure 4.5. The H-plane beamwidth in Figure 4.5 is approximately 20 degrees, and Table 4.1 below shows the expected trend of increasing directivity and decreasing beamwidth with increasing frequency. These values of beamwidth are similar to those measured for the sectoral horn (whose dimensions have been used in Figure 4.1) as shown in Table E.1 of Appendix E. The above computations were performed using the thesis code; results using the reference code (which can be applied since there is no dielectric material in the horn-only model) are virtually identical.

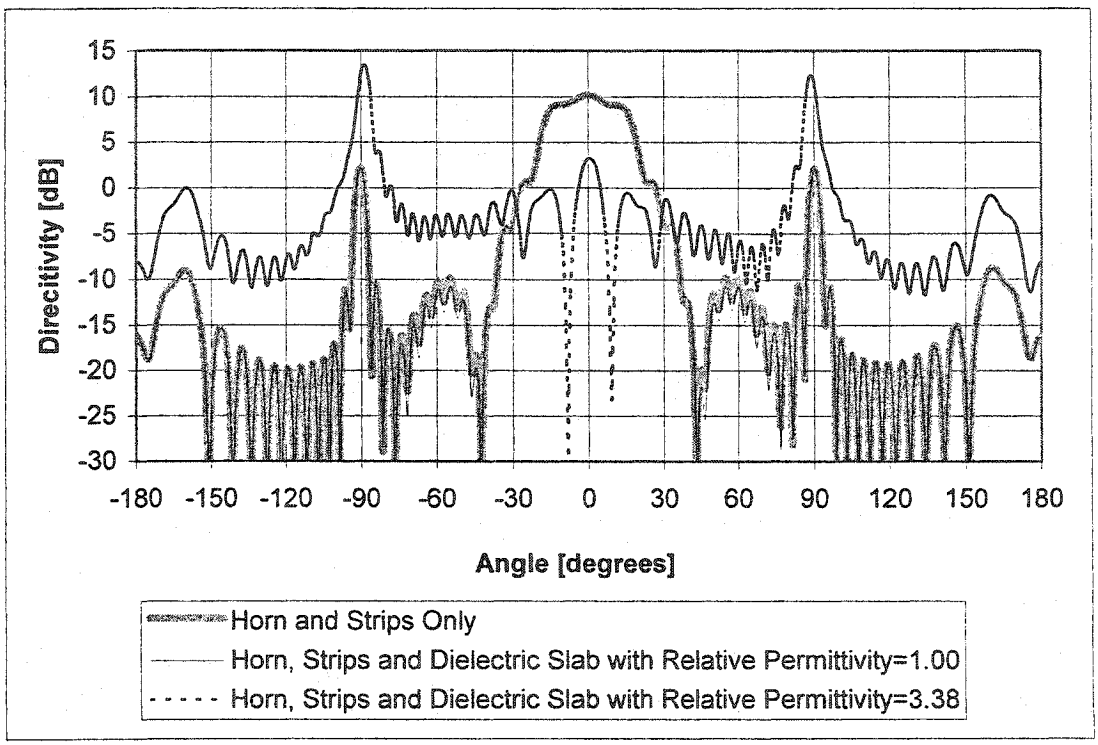

Figure 4.2: **Computed H-Plane Pattern at 30 GHz, Using the Reference Code (No Substrate), Thesis Code With ε_r=1.00 (Effectively No Substrate Present) and Thesis Code With ε_r=3.38 (the Actual Substrate Used for the Original Single-Sided Holographic Antenna).**

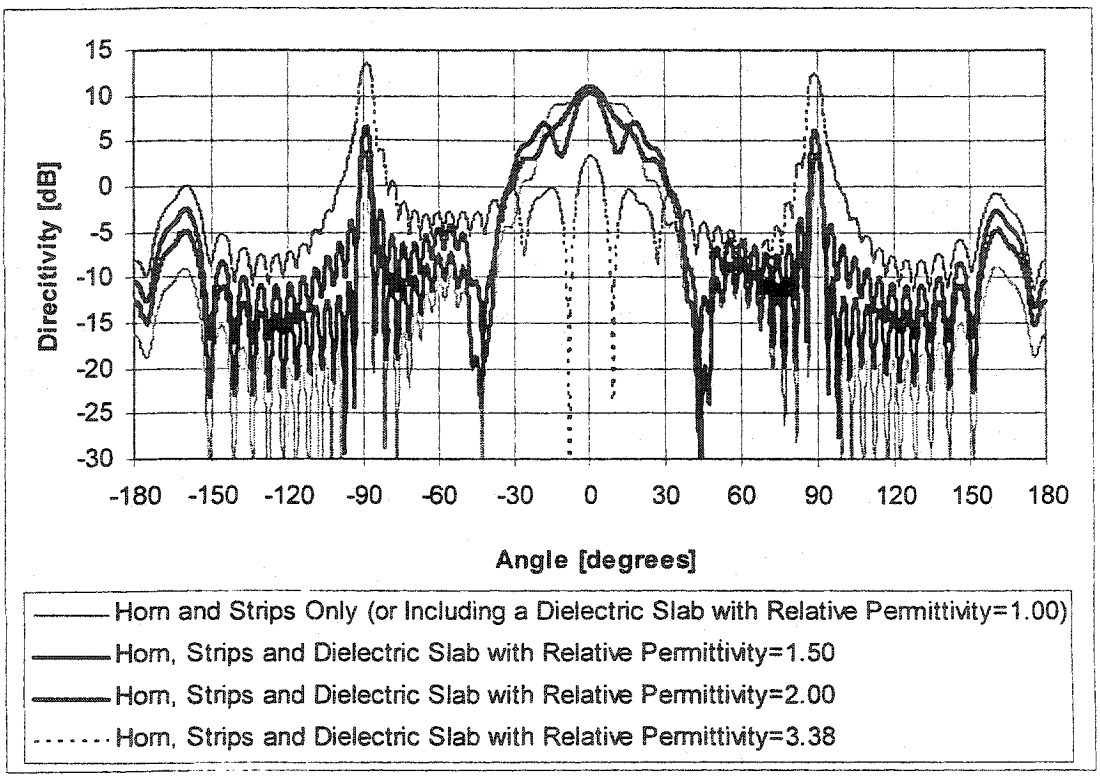

Figure 4.3: **Computed H-Plane Patterns at 30 GHz Using the Thesis Code, Showing the Effect of Gradually Increasing the ε_r of the Substrate from Unity.**

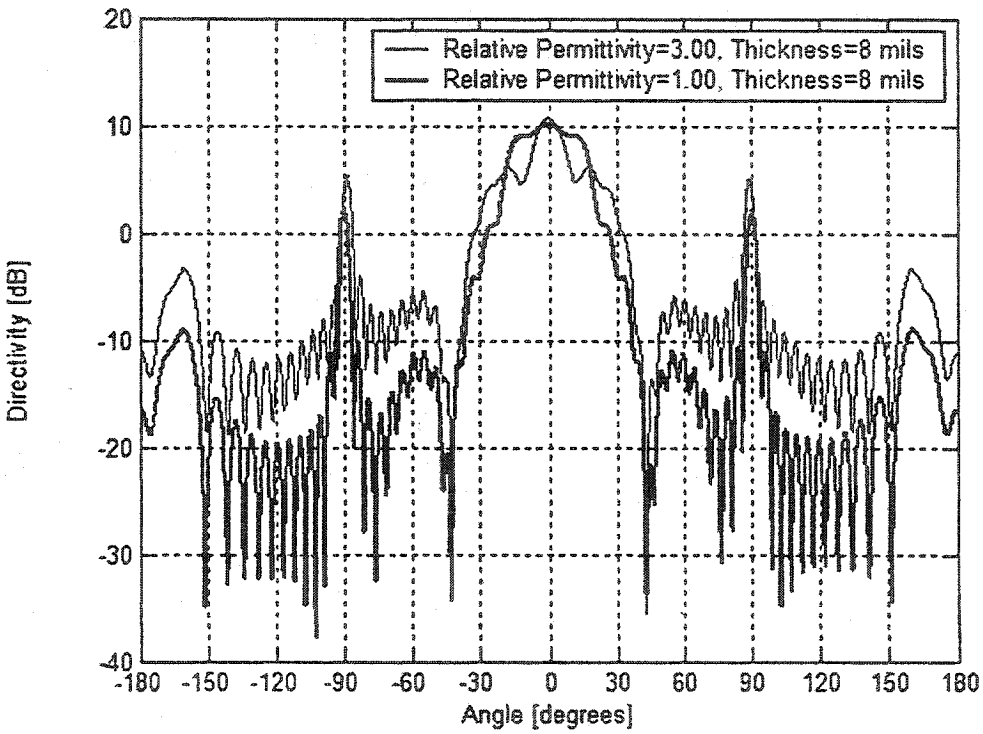

Figure 4.4: **Computed H-Plane Patterns at 30 GHz Using the Thesis Code, Showing the Influence of the Substrate Material Even for Thin Substrates.**

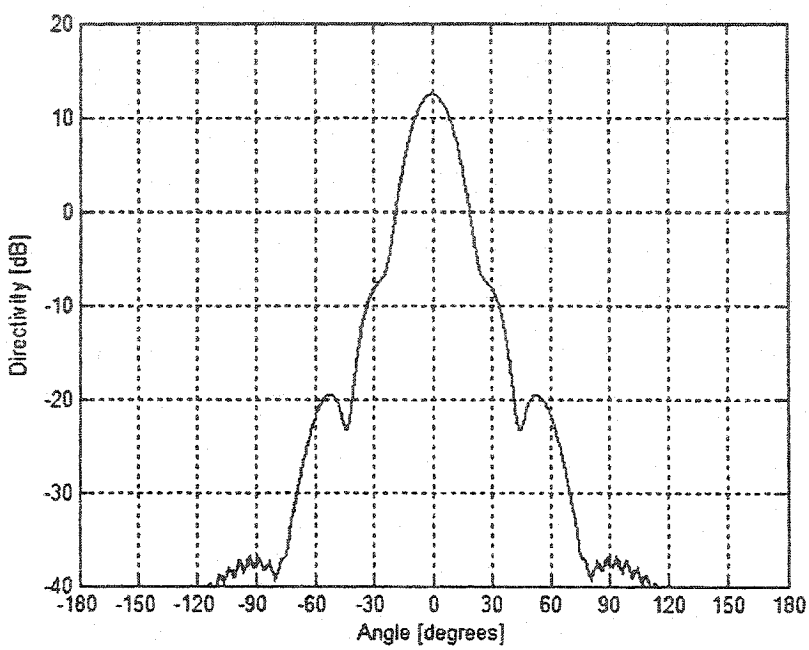

Figure 4.5: Computed H-Plane Radiation Pattern of the Sectoral Horn Antenna at 30 GHz

Table 4.1: Computed H-Plane Radiation Pattern Characteristics of the Horn Antenna Versus Frequency

Frequency [GHz]	*Maximum Two-Dimensional Directivity [dB]*	*3-dB Beamwdith [Degrees]*
24	11.60	23.6
25	11.70	22.8
26	11.90	21.8
27	12.00	21.2
28	12.20	20.4
29	12.34	19.8
30	12.50	19.0

4.4 Justification of the Two-Dimensional Formulation as an Electromagnetic Model for the Holographic Antenna H-Plane Characteristics

Comparison of computed and measured H-plane patterns for the feed horn of the holographic antenna, provided in the previous section, has already established the suitability of the electromagnetic modelling process for at least this portion of the overall holographic antenna. Figure 4.6 shows a plot of the near-zone electric field of the horn-only model along the line y = 0, for increasing x. The standing wave is observed in the waveguide portion of the horn, and the field is seen to then decrease with distance from the horn aperture as expected. Near-zone fields with a dielectric substrate present will be examined in Chapter 5. We next proceed to examine the computed and measured H-plane patterns of the complete original single-sided and double-sided antennas.

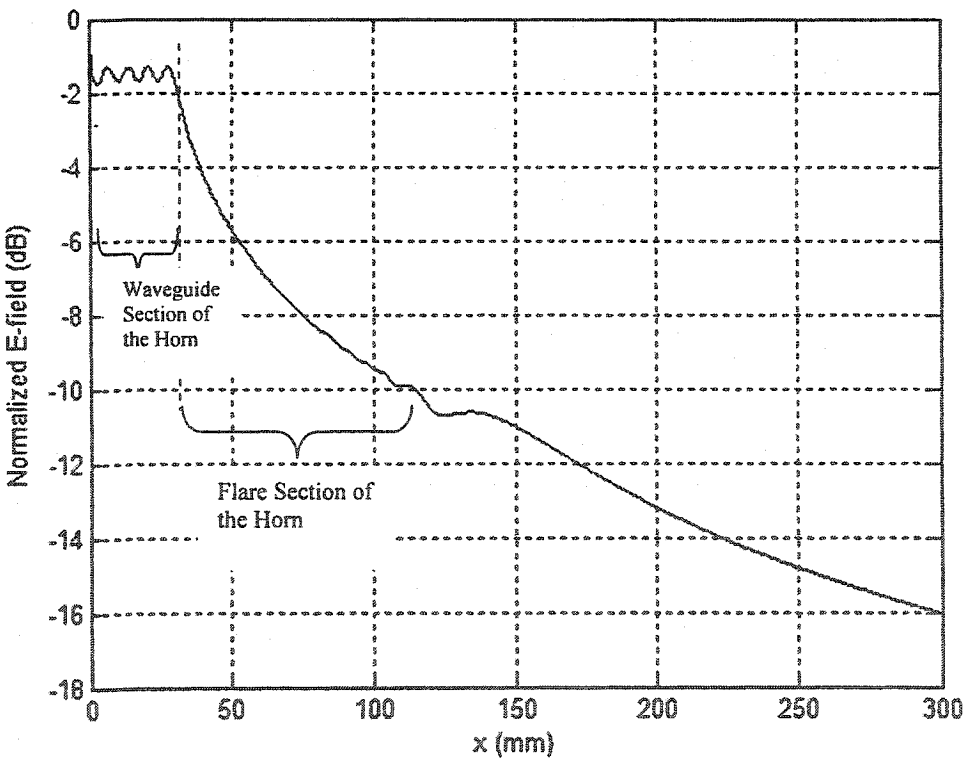

Figure 4.6: Computed Near-Zone Electric Field $|E_z|$ of the Sectoral Horn whose Radiation Pattern is Shown in Figure 4.5

A. Single-Sided Holographic Antenna

The computed pattern of the original single-sided holographic antenna, already shown in Figure 4.2, is repeated in Figure 4.7 with the other graphs removed for clarity. The measured H-plane pattern for the single-sided antenna being modelled has already been provided in Figure 2.3. The similarity in the computed and measured lobe structure is clear. The computed results do not suffer from the effects of the mounting jig used to support the antenna during measurement. Figure 4.8 compares the variation of the computed and measured angular locations of the F lobe with frequency. A linear trend is expected but the flat portion of the plots is probably due to mutual coupling between the strips. Although the computed and measured locations differ by about two degrees, the trend is the same. Further comparisons of measured and computed patterns are provided in Chapter 5.

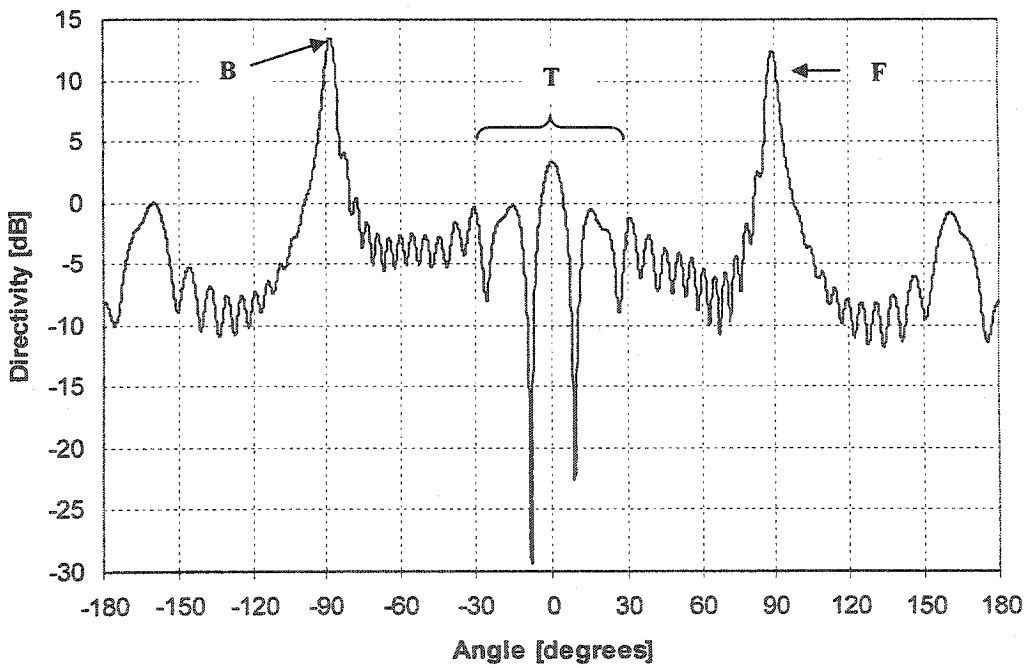

Figure 4.7: Computed H-Plane Radiation Pattern of the Original Single-Sided Holographic Antenna at 30 GHz.

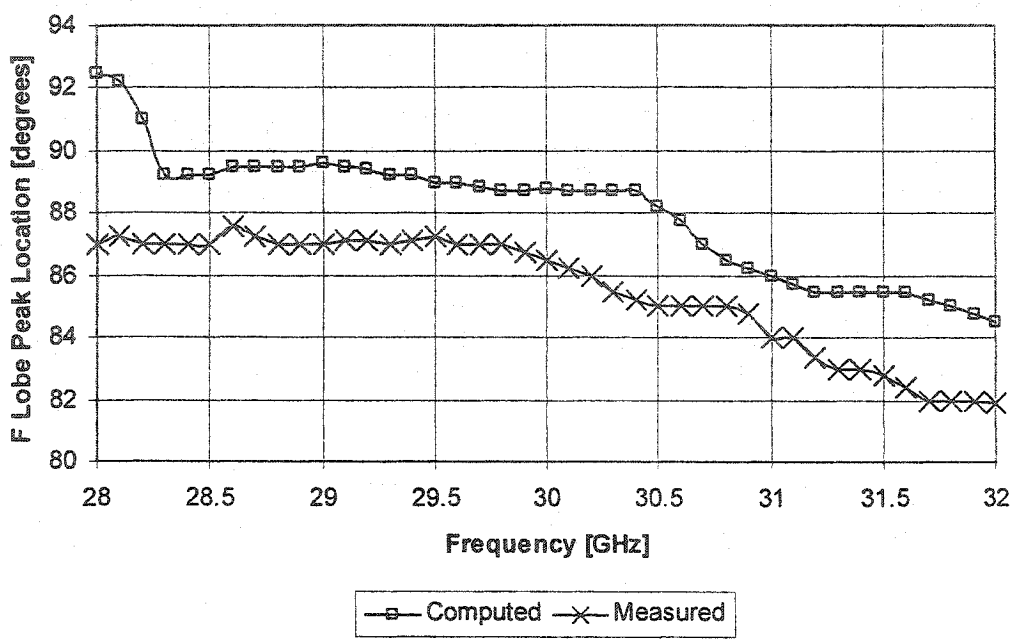

Figure 4.8: Computed and Measured F Lobe Peak Angle Location Versus Frequency for the Original Single-Sided Holographic Antenna. (The Broadside Direction is 90°).

B. Double-Sided Holographic Antenna

In most applications only one main lobe is required hence the double-sided holographic antenna. The strips on the top and bottom side of the dielectric substrate are arranged in such a way that the fields due to their currents add constructively in the directions of the F and T lobes while adding destructively in the direction of the B and S lobes. Figure 4.9 shows the computed H-plane fields of the double-sided holographic antenna. We observe immediately that the expected behaviour is exhibited by the two-dimensional model. The F lobe is about 10 dB higher than the B lobe which is also the case for the measured results in Figure 2.5. A comparison of the computed and measured angular location of the F lobe is provided in Figure 4.10. It is noted that the location of

the F lobe beam peak is away from broadside at the design frequency of 30 GHz. Further comparisons of measured and computed patterns are provided in Chapter 5.

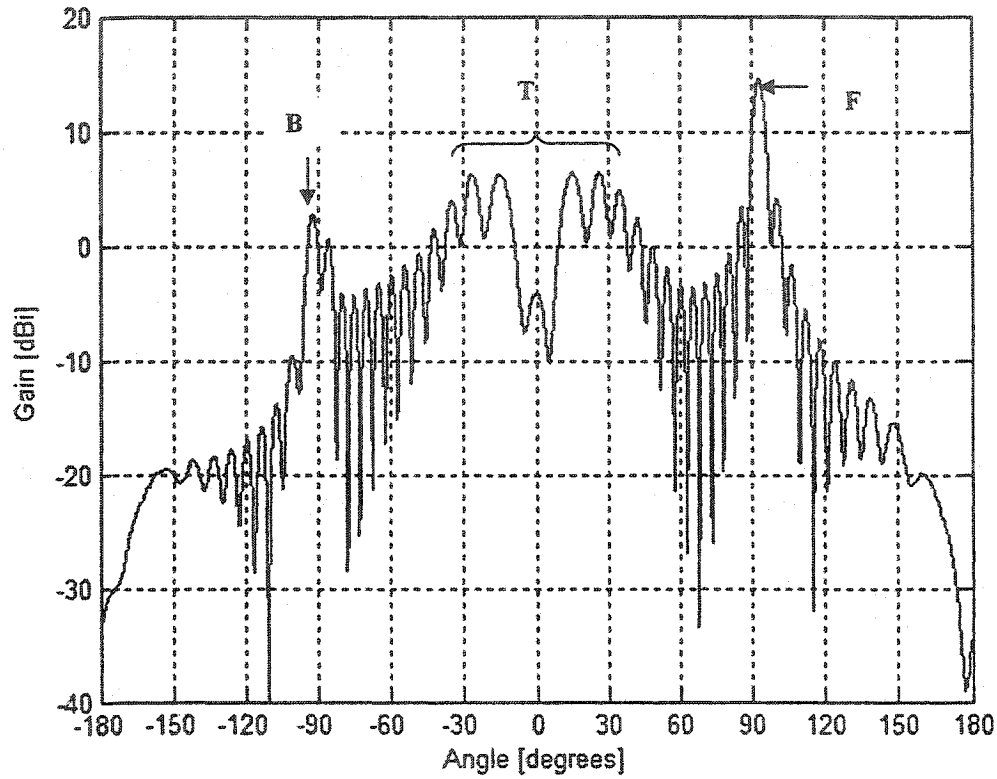

Figure 4.9: Computed H-Plane Radiation Pattern of the Original Double-Sided Holographic Antenna at 26 GHz.

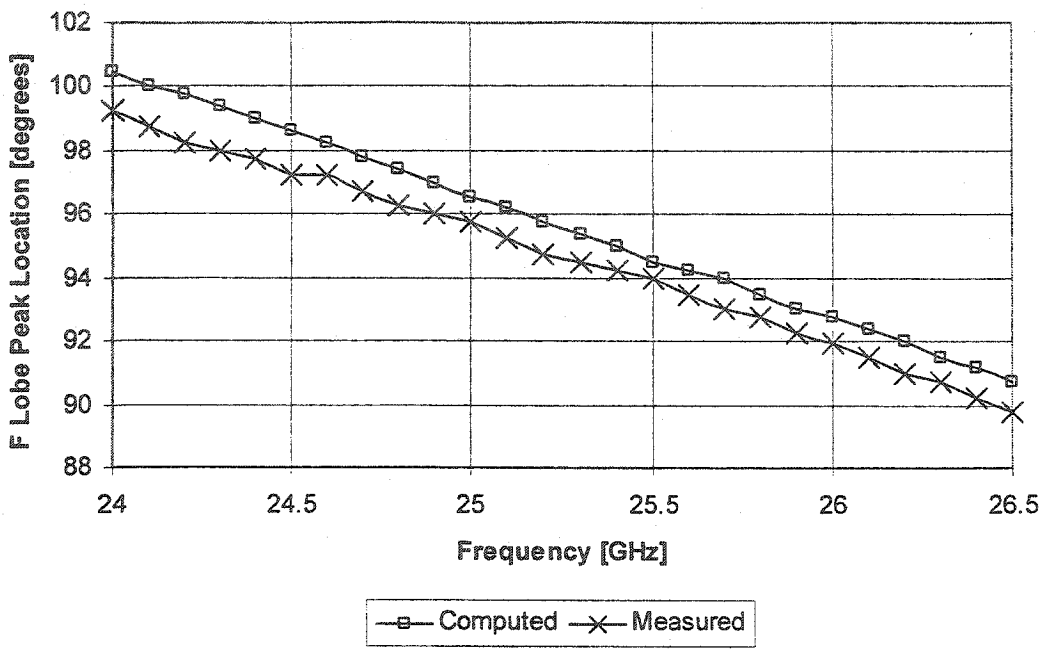

Figure 4.10: Computed and Measured F Lobe Peak Angle Location Versus Frequency for the Original Double-Sided Hologram. (The Broadside Direction is 90°).

4.5 Conclusions

In Section 4.3 of this chapter we have established correctness of the extended integral equation formulation of Chapter 3, the associated moment method formulation, and the associated code. We then, in Section 4.4, used this code to model the H-plane patterns of planar holographic antennas. Through comparison with measured H-plane pattern data from existing single- and double-sided holographic antennas, and the observation of the expected physical behaviour when certain parameters in the numerical models are altered, we have demonstrated that the two-dimensional coupled integral equation model constitutes a useful electromagnetic model for the H-plane characteristics of the holographic antenna.

4.6 References for Chapter 4

[1] L. Botha & D.A. McNamara, "Examination of antenna patterns of profiled horns using the method of moments", 1985 *IEEE AP-S Symposium Digest*, Vol.1, pp.293-296, Vancouver, Canada.

[2] D.A. McNamara & L.J. du Preez, "An integral equation approach to determine the significant design parameters of corrugated-surface travelling-wave antennas", Proceedings of the *5th International IGTE Symposium on Numerical Field Calculation in Electrical Engineering*, Technical University of Graz, Graz, Austria, pp.43-47, Sept.1992.

[3] K. Lévis, A. Ittipiboon, A. Petosa, L. Roy & P. Berini, "Ka-Band Dipole Holographic Antennas', IEE Proc.-Microwave Antennas Propagation, Vol. 148, No. 2, pp.129-132, April 2001.

[4] K. Lévis, "Ka-Band Holographic Antennas", Master of Applied Science Thesis, Faculty of Engineering, University of Ottawa, September 1999.

CHAPTER 5

Electromagnetic Modelling and Optimization of the Holographic Antennas

5.1 Introductory Remarks

In the previous chapter the electromagnetic simulation tool used to model the holographic antenna was validated. In the present chapter this will be combined with an optimization routine in an attempt to arrive at a computational design tool capable of improving the performance of initial holographic antenna designs. The original single-sided and double-sided holographic antennas will both be considered.

In all the computed results shown in this chapter we have used 20 expansion functions per free space wavelength on the horn walls and 40 per free space wavelength on the dielectric substrate. This ensures convergence. Indeed, Figure 5.1 shows a comparison of the computed radiation pattern of a single-sided antenna when the above expansion function density has been increased even further so that there are up to 3 such functions on even the narrowest strips. There is negligible difference between this excessive segmentation and that to be used in this chapter.

The measurements shown in this chapter were performed using the test jig shown in Appendix E. With the test jig mounted on the test chamber positioner, which is covered with absorber, it is possible to measure radiation patterns out to about ±120°; beyond that the antenna is blocked by the positioner and its absorber. We have therefore restricted the angular region to ±120° whenever showing measured patterns or when comparing the latter to computed results. In the remainder of the chapter by "computed" we will always mean "computed using the electromagnetic model".

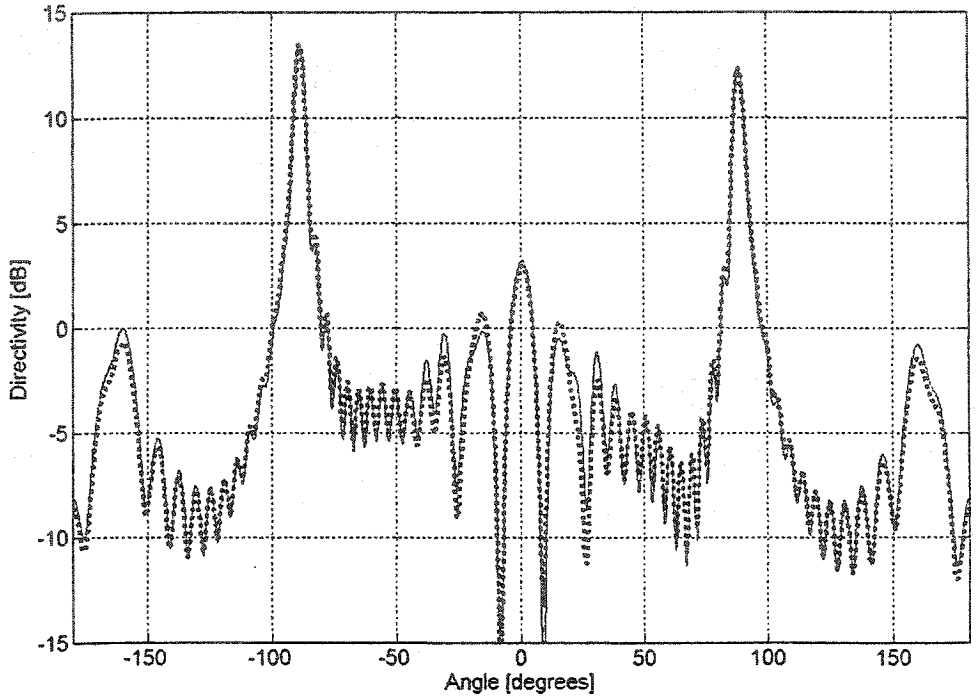

Figure 5.1: Computed H-plane Radiation Patterns of a Single-Sided Holographic Antenna Using 40 Segments Per Wavelength (——) and Almost Double That Number (•••••).

5.2 Objective Function Representing the Holographic Antenna Design Goals

In order to apply numerical optimisation it is of course necessary to translate a set of practical requirements into mathematical expressions which define the objective function to be minimized. The objective function used in this paper is simply the two-dimensional directivity function derived in Appendix C as

$$D(\phi) = \frac{|E_z(\phi)|^2}{\frac{1}{2\pi}\int_0^{2\pi}|E_z(\phi)|^2 d\phi} \tag{5-1}$$

In (5-1), $E_z(\phi)$ is the range-independent portion of the far-zone total electric field $E_z^{ext}(\underline{\rho}) = E_z(\phi)e^{-jk\rho}/\sqrt{\rho}$. The argument is that if we optimize this two-dimensional

directivity associated with the H-plane of the antenna, we will at once be optimizing the true (three-dimensional) directivity of the antenna. This will be shown to indeed be the case.

It is appropriate to remind ourselves what we will mean when comparing computed and measured radiation patterns. In the case of the two-dimensional model it is not possible to determine the true (three-dimensional) directivity; instead we calculate the two-dimensional directivity defined in (5-1). When a direct comparison is made between a computed and a measured pattern the normalized forms of each will be compared. It is possible to compare computed two-dimensional beamwidths and measured H-plane beamwidths directly.

5.3 Numerical Optimization Routines and their Integration with the Electromagnetic Model

Two optimization algorithms were used in this work, one based on a gradient method and the other on the genetic algorithm.

The gradient method was implemented using the commercially available routine *LCONF* [1] to perform numerical optimization of both the single-sided and double-sided original antennas. This routine is able to minimize a multivariable user-defined function subject to user-specified "simple bounds" [1] on the optimization variables, as well as user-specified equality and/or inequality constraints. In the present case, for an antenna consisting of N conducting strips, the variables are the conducting strip widths $\{w_1, w_2, ..., w_N\}$ and locations $\{d_1, d_2, ..., d_N\}$ of the strip centres from some selected reference point. The user-defined function is then

$$F(w_1, w_2, ..., w_N, d_1, d_2, ..., d_N) = -10\log\{D(\phi_o)\} \quad (5\text{-}2)$$

with ϕ_o a specified value of ϕ. At each step in the execution of the optimization process the algorithm has a set of strip widths and locations that are used to compute $E_z(\phi_o)$, and hence the objective function, using the electromagnetic model. The simple bounds ability is used to define the allowable range of strip widths (e.g. for the fabrication process used in this paper the minimum strip width is 10 mils or 0.254 mm). The linear inequality constraints ability is used to ensure that during optimization the algorithm does not cause the strips to overlap. For example, the spacing between the first and the second strip cannot be less than zero and its linear inequality constraint can be written as $d_2 - d_1 - \frac{w_1}{2} - \frac{w_2}{2} \geq 0$. Routine *LCONF* also requires the user to specify initial values ("guesses") for the w_n and d_n. In the case of the original single-sided holographic antenna we have N = 13 (and hence a total of 26 optimisation variables), whereas for the double-sided case N = 26 (and hence there are 52 optimisation variables). The optimization process was repeated many times for both the above antennas with different starting points. In this thesis we have selected $\phi_o = 90°$. The optimization is performed at 30 GHz for the single-sided antenna and at 26 GHz for the double-sided antenna. The 30 GHz was selected for the single-sided antenna because the original antenna [2] had the highest F-lobe at this frequency. The 26 GHz was selected for the double-sided antenna because the original antenna [2] had the highest F/B ratio at this frequency.

The FORTRAN code which implements the genetic algorithm was obtained from [3]. An in-depth description of the way this evolutionary algorithm functions is provided in [4], and so further details need not be discussed here. The particular genetic algorithm

used allows simple bounds on the optimization variables but not general linear inequality constraints. Thus the simple bonds have to be used to ensure that the conducting strips do not overlap during optimization; this results in the range of values of the strip widths and strip locations being more restrictive than when using the gradient algorithm.

The gradient algorithm was always found to obtrude an optimized antenna whose peak directivity was slightly higher than those obtained from the genetic algorithm. This is perhaps not surprising since it uses as starting values the dimensions obtained using the procedure in [2], whereas the genetic algorithm since starts with randomly selected values. The gradient method is also much more rapid. The drawback of the gradient method is usually stated as being that it may fall into a local minima and the result not the globally optimum value. However, given the additional physical understanding possible through performing a number of key analyses for the holographic antenna, local minima can be largely avoided. Furthermore, in spite of the major reduction in computational time due to the use of a 2D simulation model, computation times are still long. For instance, when optimizing the single-sided antenna (i.e. with 26 optimisation variables) using the gradient algorithm approximately 2400 simulations are required. The optimization process was repeated many times for the single-sided hologram using the gradient method, genetic algorithm method and a combination of these two. They were also repeated with different starting points and other algorithm-related optimization parameters embedded in the routines. Only the gradient method was used for the double-sided hologram as it has twice the number of variables compared to the single-sided hologram and optimization using genetic algorithm proved to be difficult. Thus we have

settled on the use of the gradient algorithm for all the results presented in this thesis. Only the best results from these optimizations are presented.

5.4 Optimization of the Original Holographic Antenna

5.4.1 The Optimized Single-Sided Holographic Antenna

The computed (two-dimensional) directivities of the original and optimized single-sided antennas are shown in Figure 5.2. The corresponding comparison of measured gains is presented in Figure 5.3. It is clear that the optimized antenna has an improved performance but that the frequency band over which this occurs is slightly narrower than expected from Figure 5.2. One possible reason for the computed performance being more "optimistic" might be related to the effect of the horn position relative to the dielectric slab. Figure 5.4 shows computed directivities of the optimized antenna for various positions of the feedhorn aperture with respect to the edge of the dielectric substrate. The 0.0 millimetre location is the one used in the optimization process. It is observed that as the location is altered there is a change in the frequency at which the highest directivity occurs. In the actual antennas the feedhorn "sees" an angled portion of the substrate (as can be observed in Figure 2.1), whereas in the two-dimensional model it does not. Thus it is difficult to determine precisely what the feedhorn location must be in the theoretical model in order to correspond to a specific situation in the actual antenna.

Figure 5.5 gives a chart which compares the widths of the conducting strips for the original and optimized antennas. The optimization process has increased the width of

the strips furthest from the feed horn. The computed (near-zone) magnitude of the electric field $E_z(x, y = 0)$ along the centre-line through the dielectric substrate, shown in Figure 5.6, is revealing. In the case of the optimized antenna this field is larger further out than it is in the original (constant-strip-width) antenna. The total conducting current on each strip, obtained by integrating the true conduction current density across each strip, is shown in Figure 5.7. This also manifests the fact that the optimized antenna has achieved an increased directivity by ensuring that the strips are all more uniformly excited.

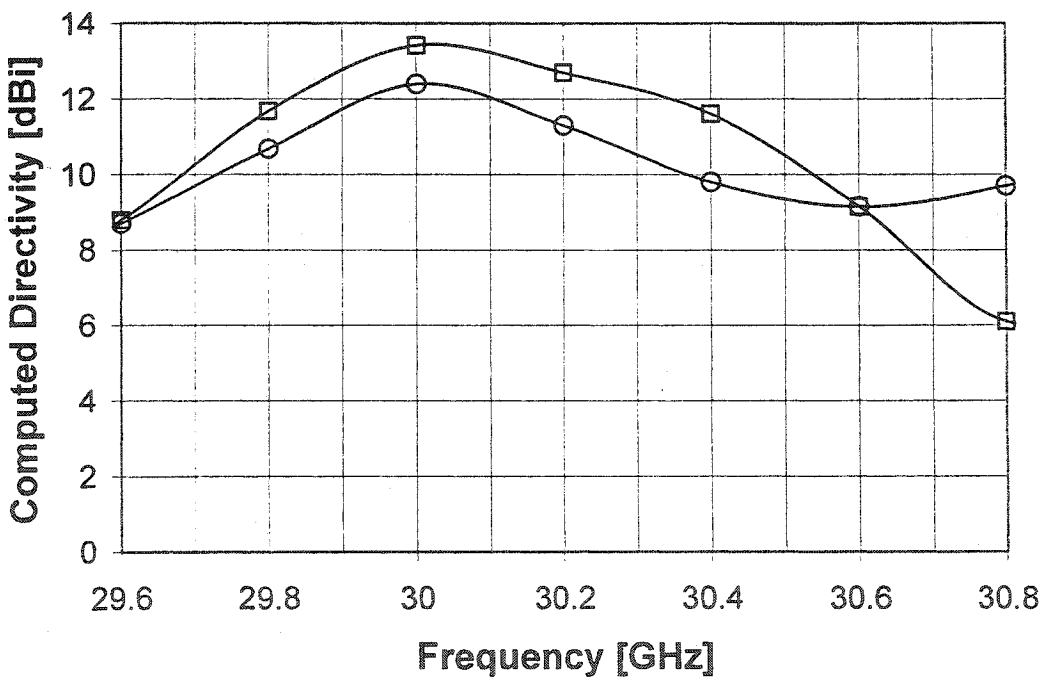

Figure 5.2: Computed Directivity of the Original (o-o-o-o) and Optimized (-□-□-□-□-) Single-Sided Holographic Antennas.

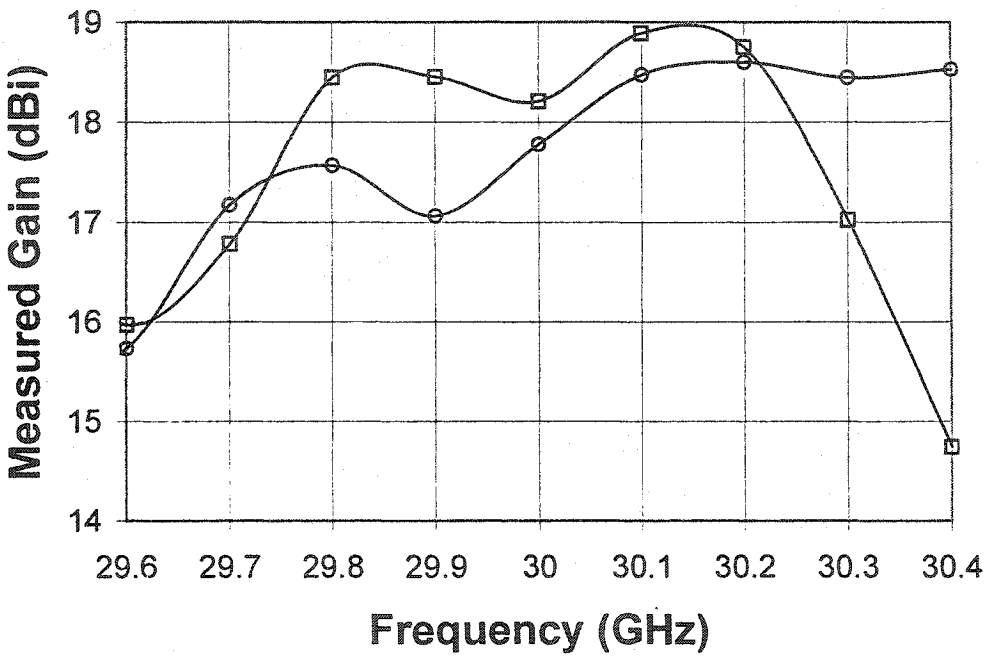

Figure 5.3: **Measured Gains of the Original (o-o-o-o) and Optimized (-□-□-□-□-) Single-Sided Holographic Antennas. (The Return Loss of Each of the Antennas was Measured and the Measured Gains Corrected for Reflection Loss).**

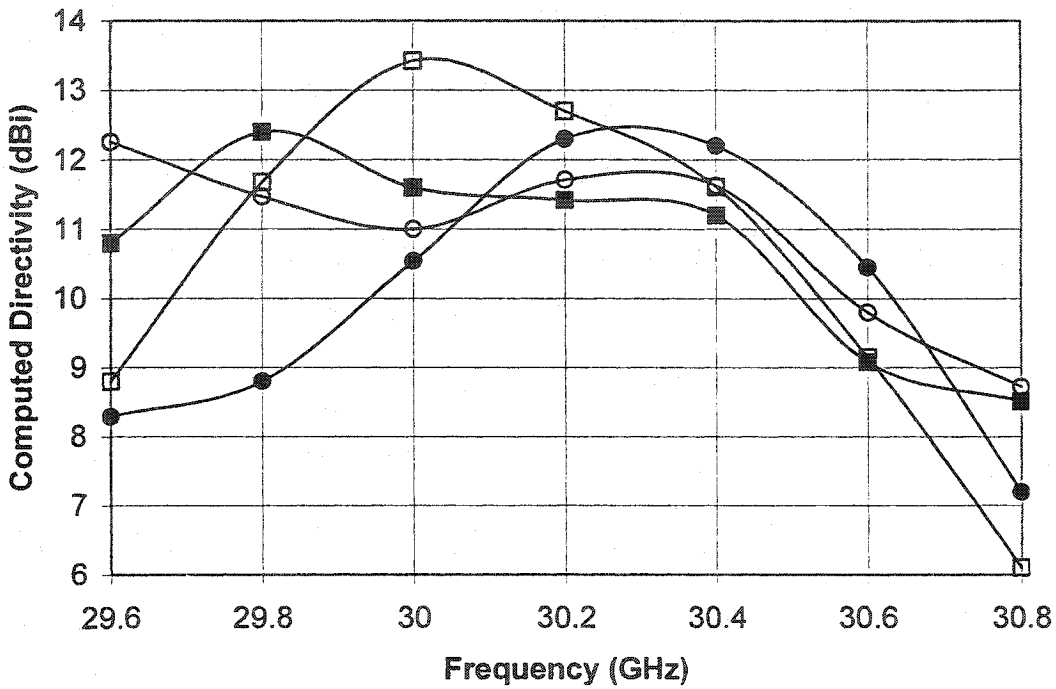

Figure 5.4: **Computed Directivity of the Optimized Single-Sided Holographic Antenna F-Lobe Peak for Feedhorn Displacements of +1mm (■-■-■-■), 0mm (□-□-□-□), -2mm (●-●-●-●) and –4mm (o-o-o-o). (A Negative Displacement Implies That the Horn is Moved Closer to the Substrate).**

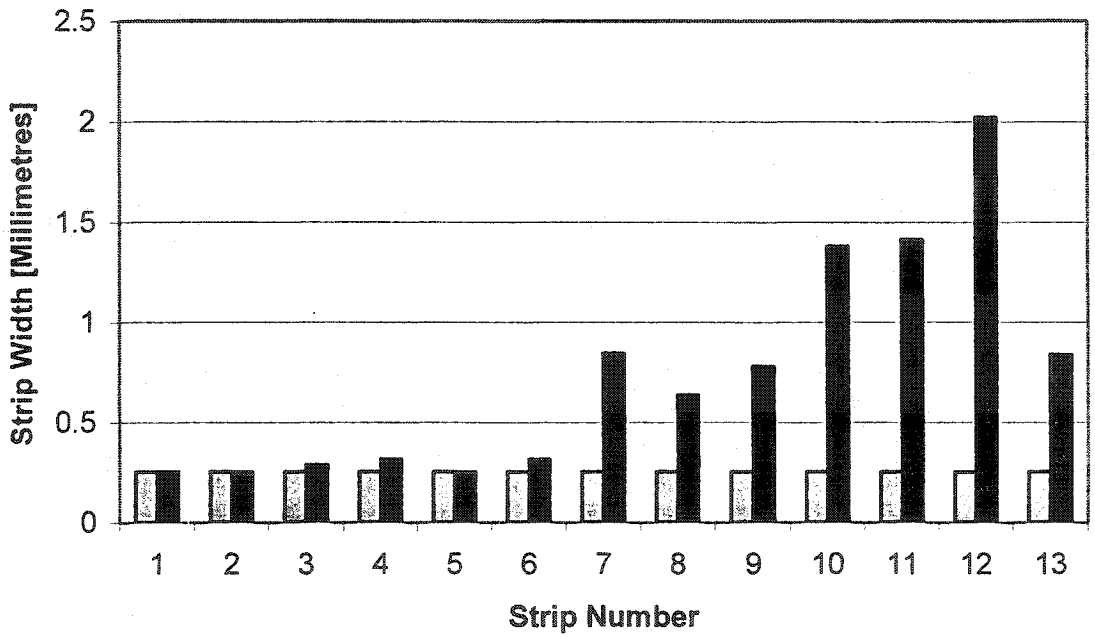

Figure 5.5: **Widths of the Conducting Strips for the Original (Hatched) and Optimized (Dark) Single-Sided Holographic Antennas.**

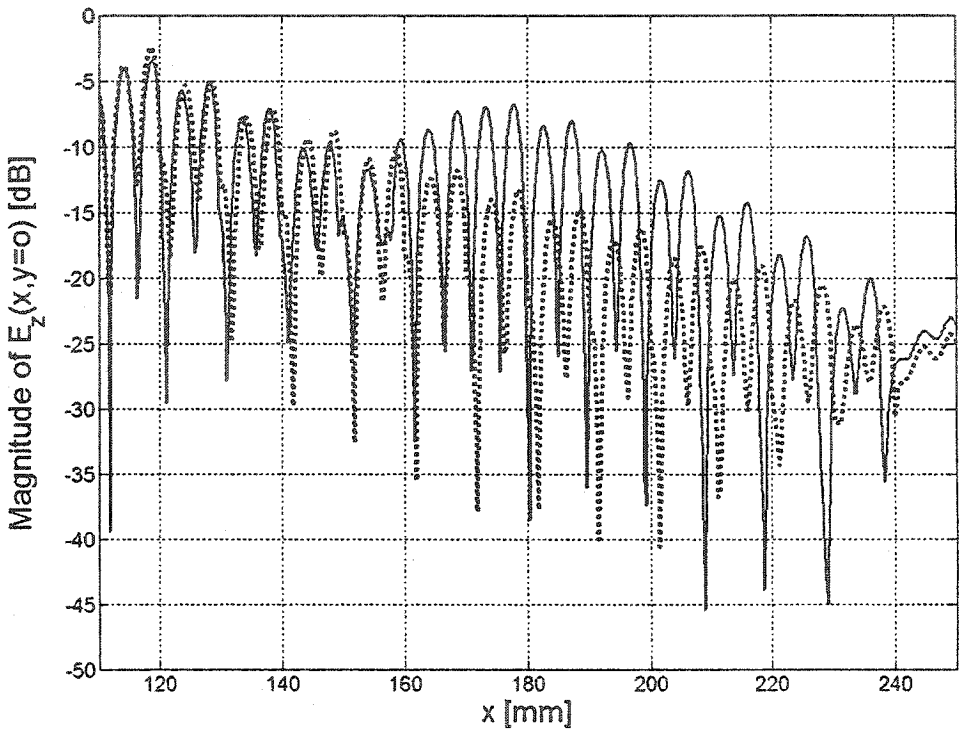

Figure 5.6: **Computed $|E_z(x,y=0)|$ in the Substrate of the Original (•••••) and Optimized (——) Single-Sided Holographic Antenna Along a Line (y = 0) Passing Through the Centre of the Substrate. The Field has been Normalized to its Maximum Value which Occurs in the Feed Horn Waveguide Region, but which has not been Shown here.**

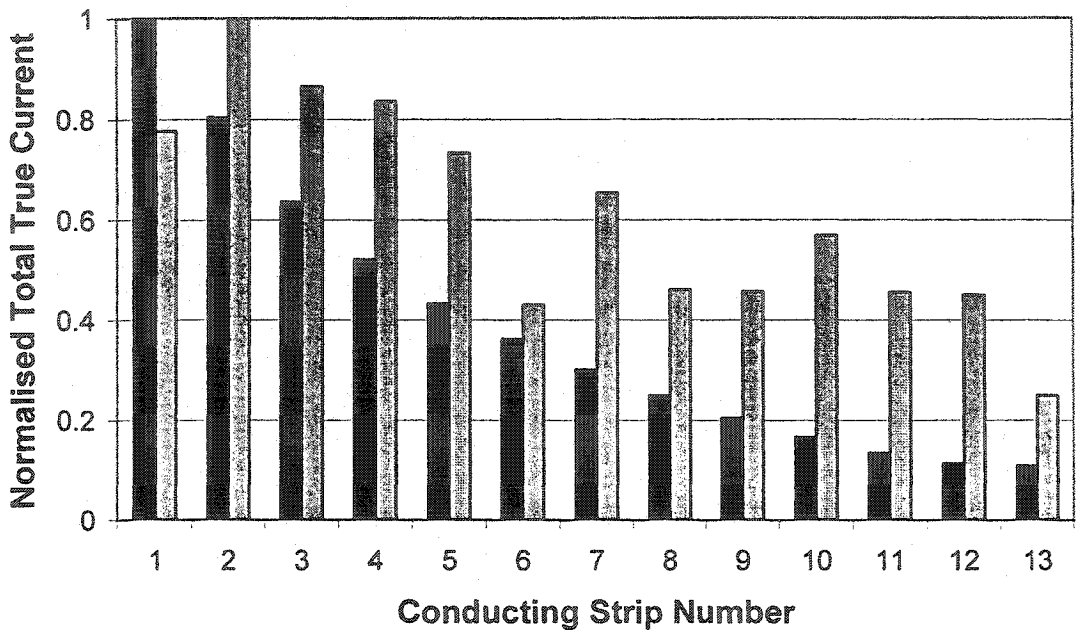

Figure 5.7: Computed Normalized True Currents on Each of the Conducting Strips for the Original (Dark) and Optimized (Hatched) Single-Sided Holographic Antennas.

Figure 5.8 shows computed radiation patterns of the original and optimized antennas at 30 GHz, and Figure 5.9 shows the measured radiation pattern of the original and optimized antennas at 29.9 GHz. One can observe the higher F lobe peak level of the optimized design in comparison to the original design as expected. However, at the out-of band frequency of 29.6 GHz, the F lobe level of the optimized antenna is not higher than the original antenna's peak as observed in Figure 5.10 and 5.11 below.

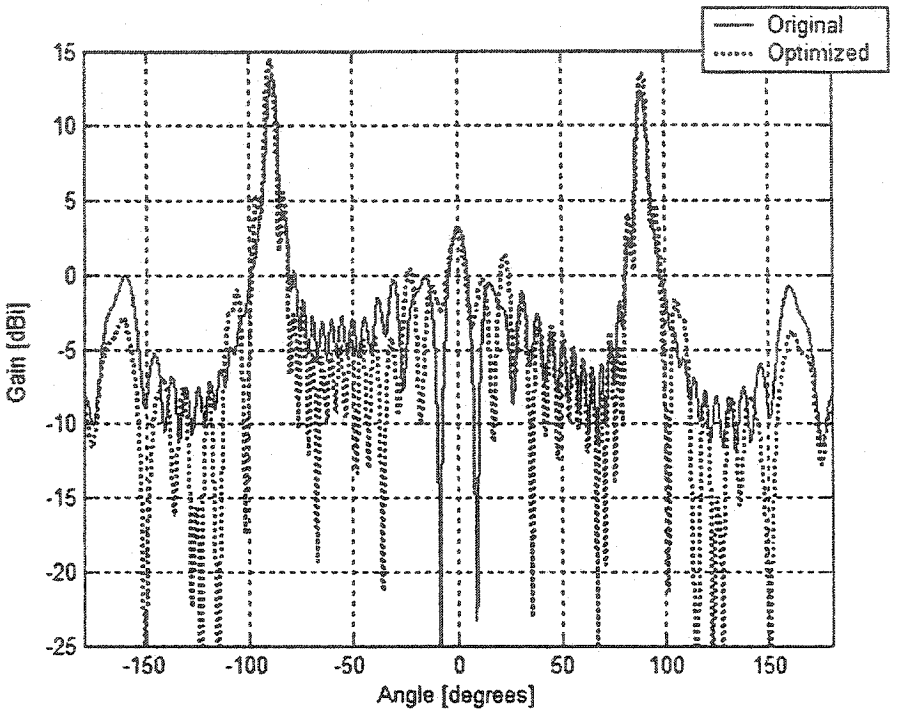

Figure 5.8: **Computed H-Plane Radiation Patterns of the Original and Optimized Single-Sided Holographic Antennas at 30 GHz**

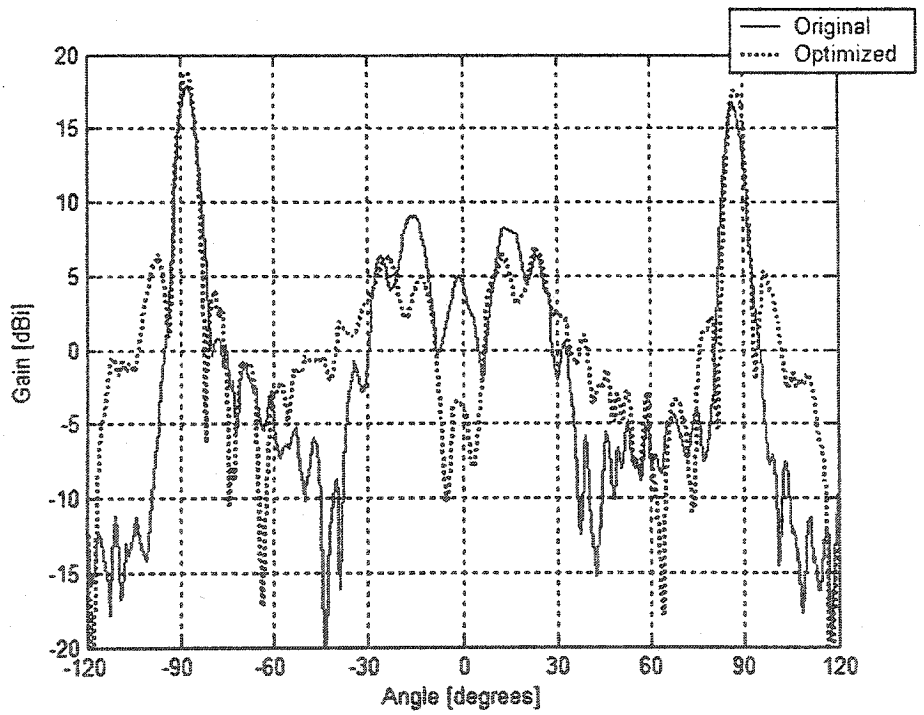

Figure 5.9: **Measured H-Plane Radiation Patterns of the Original and Optimized Single-Sided Holographic Antennas at 29.9 GHz**

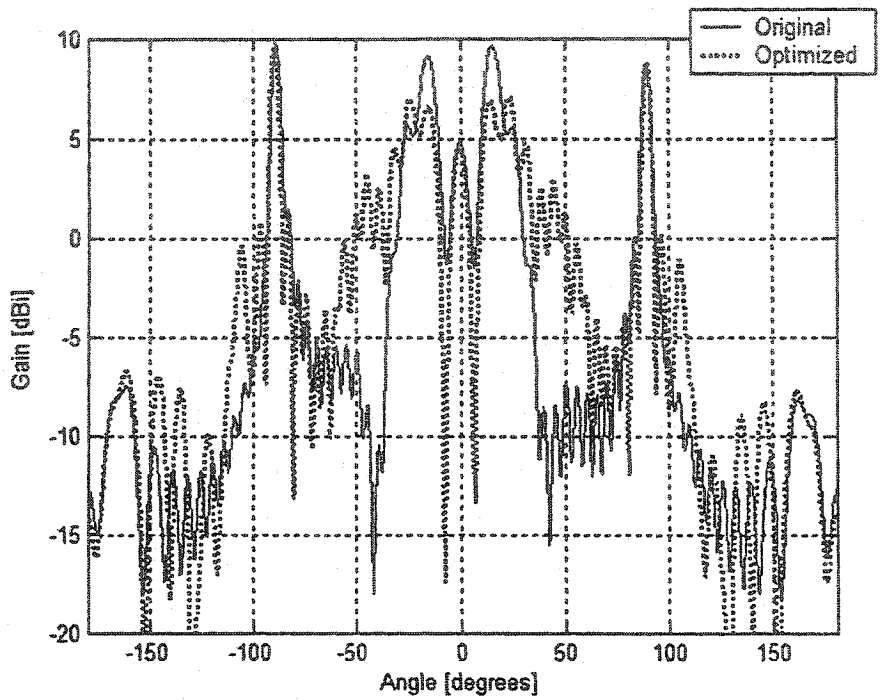

Figure 5.10: Computed Out-of-Band (29.6 GHz) H-Plane Radiation Patterns of the Original and Optimized Single-Sided Holographic Antennas.

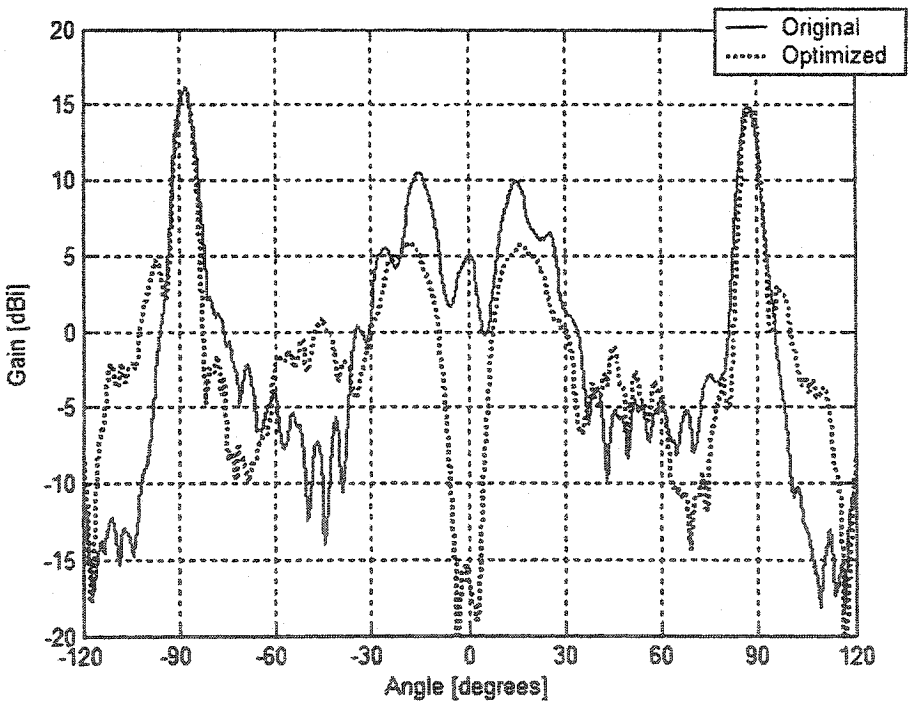

Figure 5.11: Measured Out-of-Band (29.6 GHz) H-Plane Radiation Patterns of the Original and Optimized Single-Sided Holographic Antennas.

Figure 5.12 shows the frequency variation of the computed F lobe peak locations for the original and optimized single-sided antennas. It can be observed that the "computed" peak of the optimized antenna, when compared to the original antenna, is much closer to broadside at the optimization frequency of 30 GHz. Figure 5.13 compares the variation of the computed and measured angular locations of the F lobe of the optimized antenna, with frequency. Comparing this to Figure 4.8, a similarity in the difference between the computed and measured results is observed. One can also see from Figure 4.8 and 5.13 that, at 30 GHz, the "measured" peak of the optimized antenna is closer to broadside than that of the original antenna.

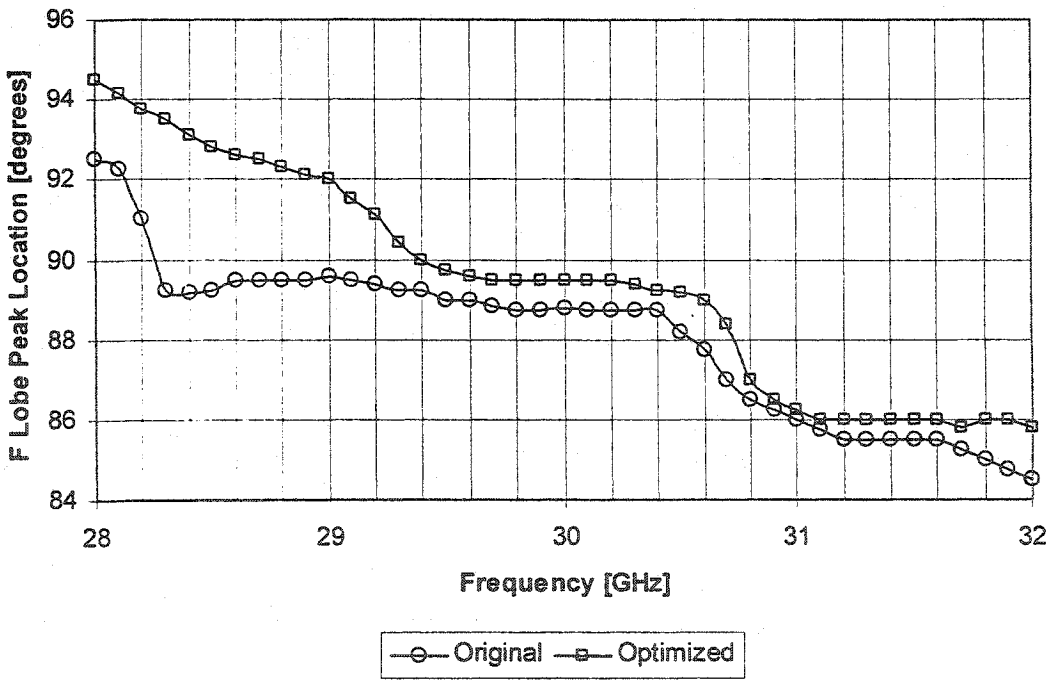

Figure 5.12: Computed F lobe Peak Angle Location Versus Frequency for the Original and Optimized Single-Sided Holographic Antenna.

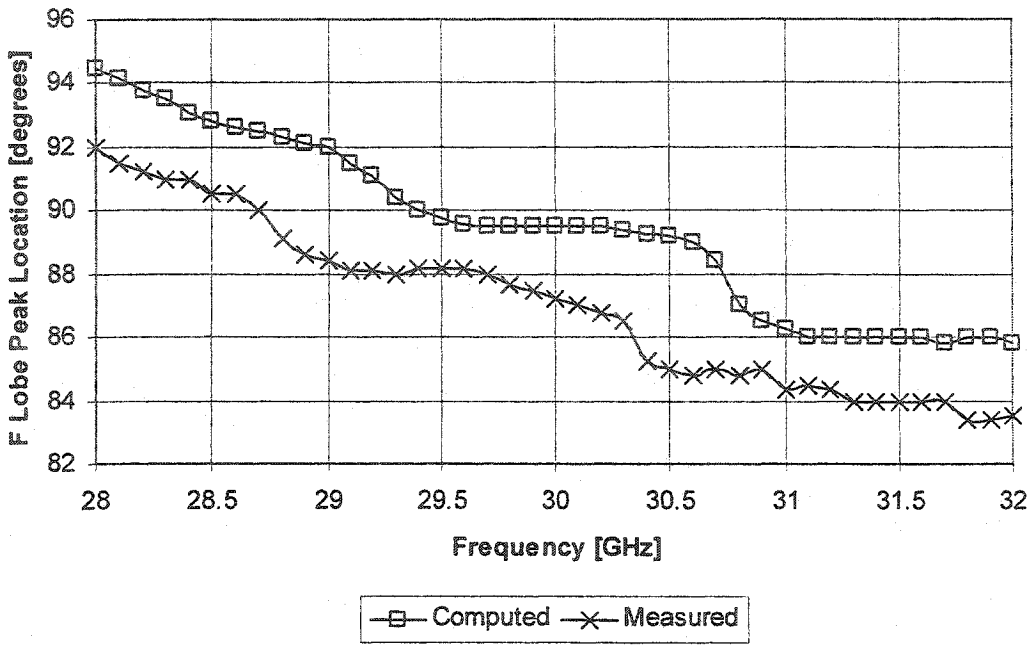

Figure 5.13: Computed and Measured F Lobe Peak Angle Locations Versus Frequency for the Optimized Single-Sided Holographic Antenna.

5.4.2 The Optimized Double-Sided Holographic Antenna

We next consider the optimization of the double-sided holographic antenna. Comparisons of the computed and measured performance for the original and optimized antennas are provided in Figures 5.14 and 5.15, respectively. The computed results indicate that the optimized antenna should have the highest directivity at 26 GHz; this is expected since it is the frequency at which the optimisation was performed. The measured data, on the other hand, shows the highest gain performance at 26.4 GHz. This shift of about 0.4 GHz is likely due to the feed location effects previously discussed for the single-sided antenna. In spite of this, it is clear that through appropriate use of the optimisation algorithm in conjunction with the electromagnetic model of the antennas it is possible to appreciably increase the gain of the holographic antenna. Measured and

computed normalized radiation patterns for the antenna at 26 GHz and 25.6 GHz (out-of-band) are shown in Figure 5.16 and 5.17, respectively. Comparing the two figures, it can be observed that the performance of the antenna at out-of-band frequencies is not as good (higher B and T lobe levels at 26.4 GHz) as those within the band i.e. 26 GHz.

Figure 5.18 shows a chart which compares the widths of the conducting strips for the original and optimized double-sided antennas. As in the case of the single-sided antenna, it can be observed that the majority of the conducting strips (with the exception of strip number 2 on the top layer) with the larger widths lie furthest from the feedhorn.

If we account for a loss of about 0.16 dB in the length of waveguide connected to the feed horn, plus a connector loss of approximately 0.2 dB, the efficiency (essentially the product of the aperture efficiency and radiation efficiency) of the double-sided holographic antenna is seen to be 23%. If we were to increase the size of this antenna to the "maximum" to be found in Figure 6.9 of Chapter 6 (namely 43 strips), it is expected that this efficiency would be maintained. In the case of a microstrip array such increased size leads to greatly decreased efficiency due to feed line loss. Extrapolating the results from [5], a microstrip array of the same size would have an efficiency of approximately 13%. Thus the holographic antenna would have some advantage over that of the microstrip array.

Figure 5.19 shows the variation with frequency of the computed and measured F lobe peak angular locations for the optimized double-sided antennas. Comparing this with the original antenna results in Figure 4.10, we can say that for both the computed and measured results, the F lobe peak of the optimized antenna is closer to broadside than that of the original antenna at 26 GHz.

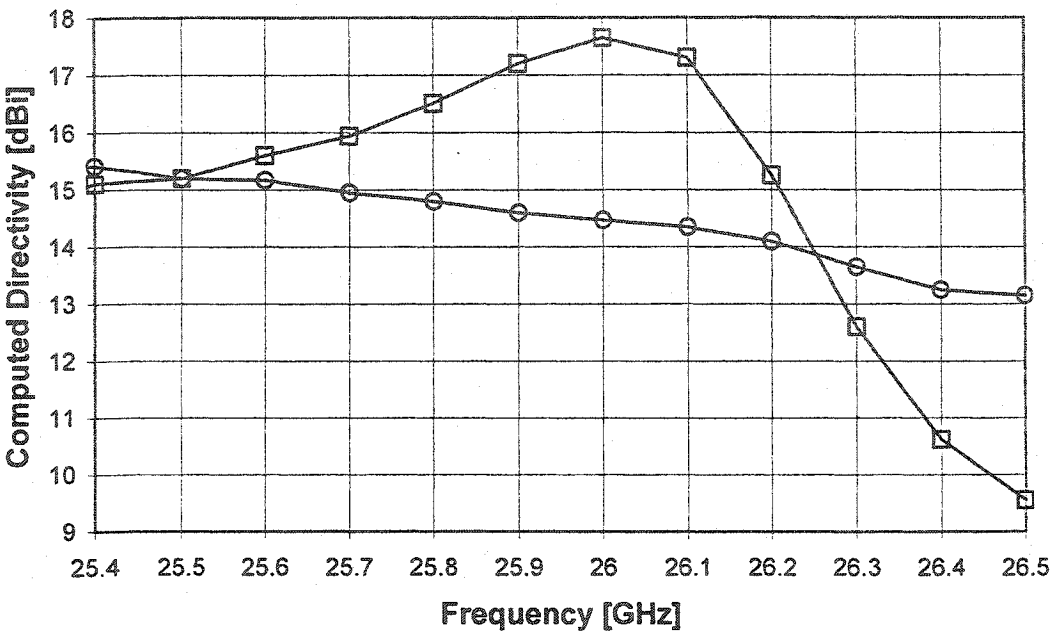

Figure 5.14: Computed Directivity of the Original (o-o-o-o) and Optimized (□-□-□-□) Double-Sided Holographic Antennas.

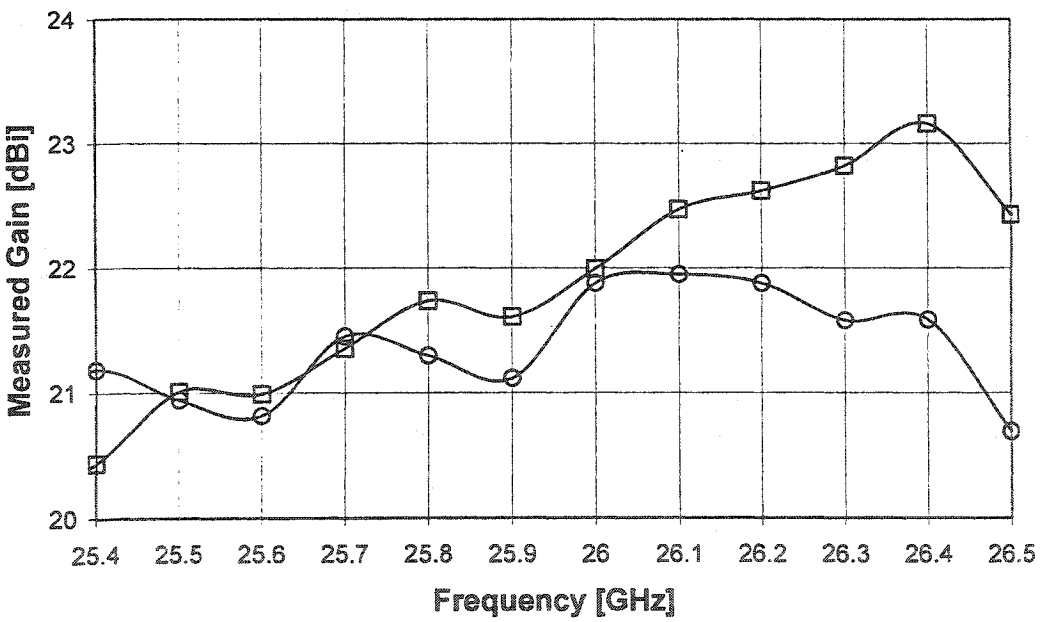

Figure 5.15: Measured Gains of the Original (o-o-o-o) and Optimized (□-□-□-□) Double-Sided Holographic Antennas. (The return Loss of Each of the Antennas was Measured and the Measured Gains Corrected for Reflection Loss).

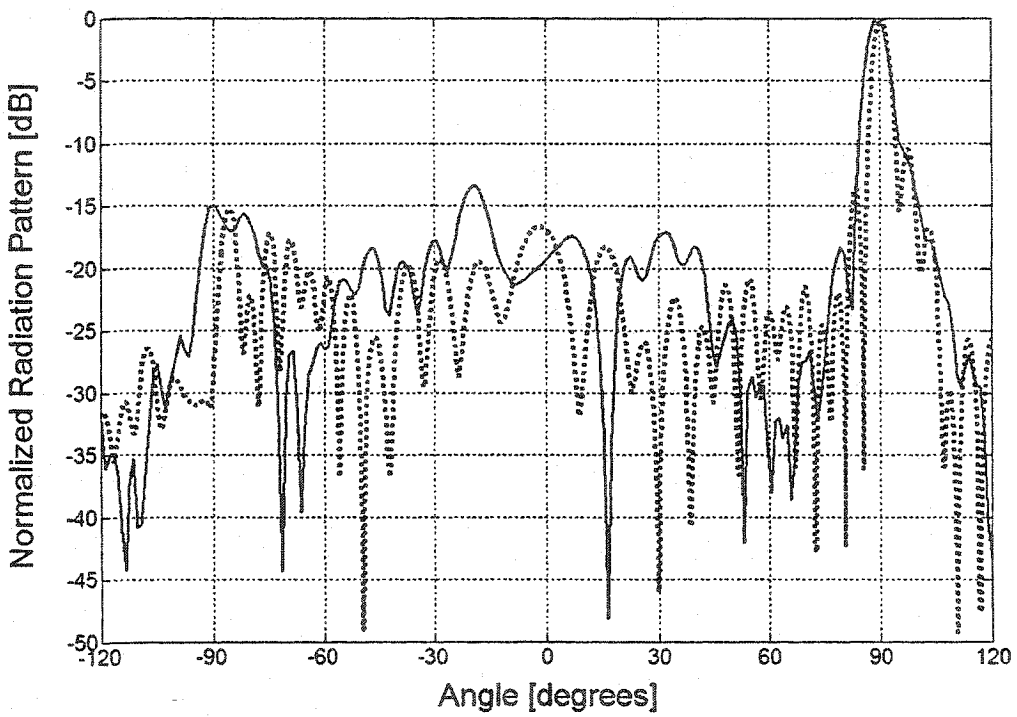

Figure 5.16: Normalised Measured (——) and Computed (•••••) H-Plane Radiation Patterns for the Optimized Double-Sided Holographic Antenna at 26 GHz.

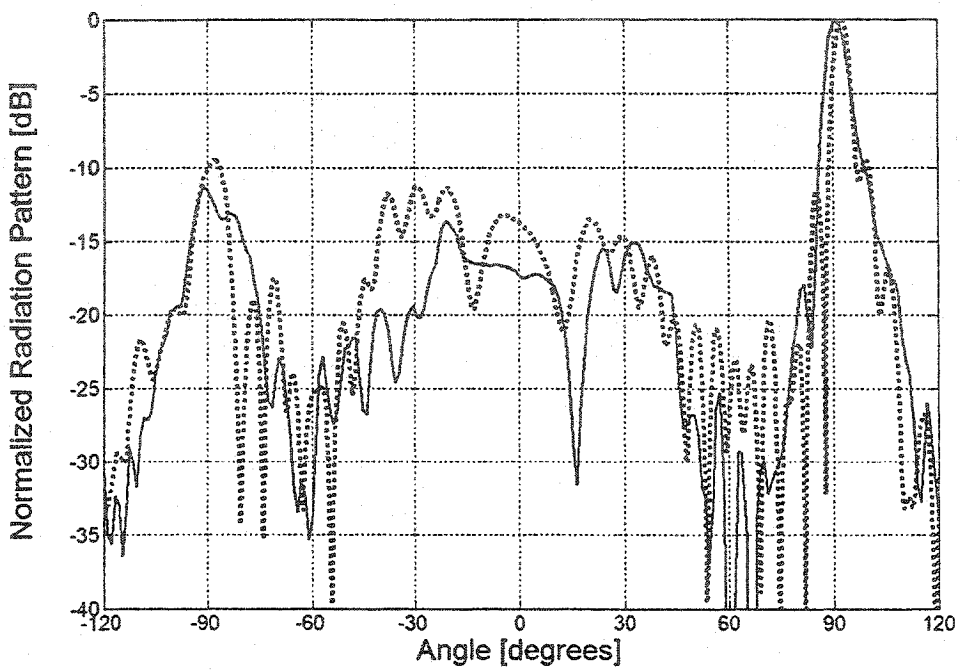

Figure 5.17: **Normalised Measured (——) and Computed (•••••) H-Plane Radiation Patterns for the Optimized Double-Sided Holographic Antenna at 25.6 GHz (Out-of-Band).**

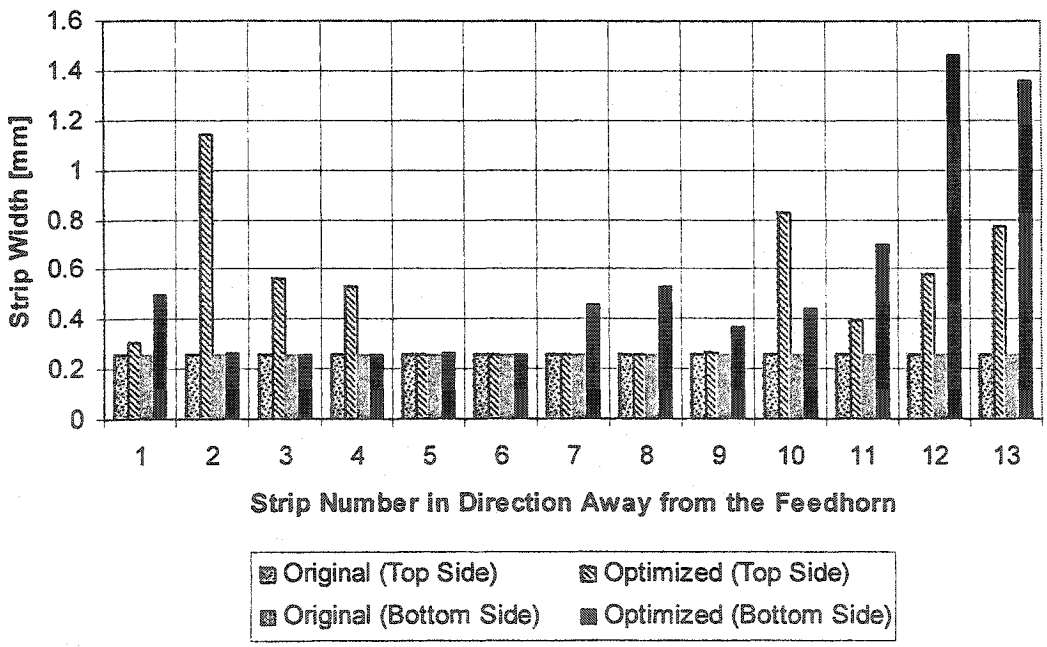

Figure 5.18: **Widths of the Conducting Strips for the Original and Optimized Double-Sided Holographic Antennas.**

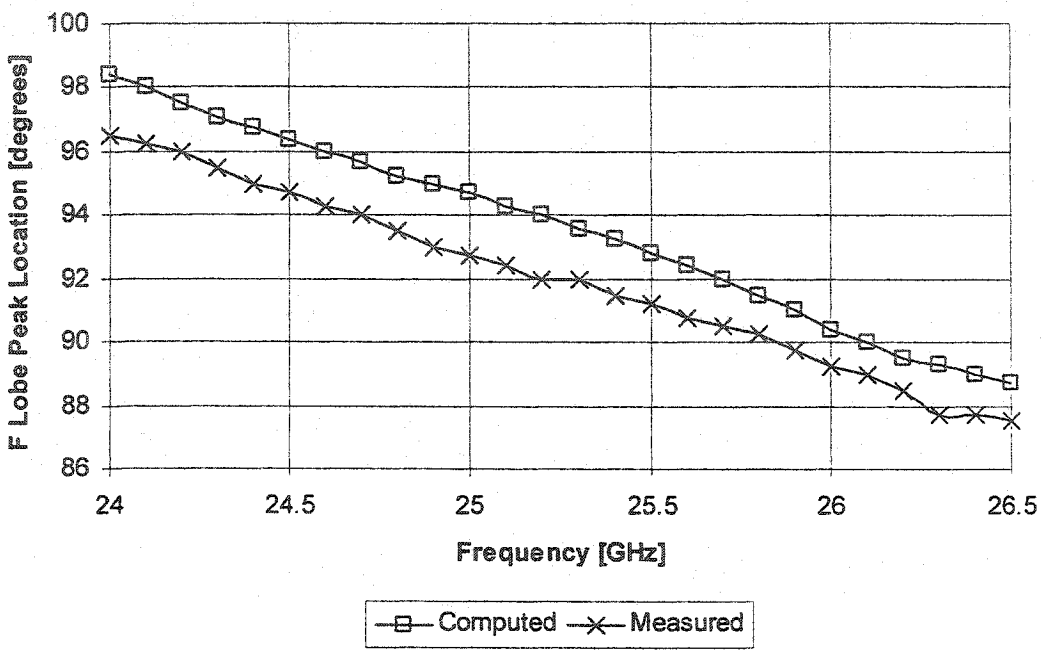

Figure 5.19: Computed and Measured F Lobe Peak Angle Locations Versus Frequency for the Optimized Double-Sided Holographic Antenna.

5.5 Conclusions

The electromagnetic model developed in Chapter 3 has been combined with a numerical optimization algorithm. This has been used to demonstrate that it is possible to vary the strip widths and strip locations of both single-sided and double-sided holographic antennas (of a fixed number conducting strips) in order to obtain higher F-lobe directivity. This has been validated experimentally. It was observed that the application of the optimization process improves the peak gain of the antenna over a frequency band on either side of the optimization frequency. However, the optimized antennas have a narrower bandwidth than the unoptimized ones designed according to the method of [2]. The near-zone analysis capability of the electromagnetic model has been used to interpret the dimensional changes brought about by the optimization process. In

the following chapter we will use the electromagnetic model to examine the effect of the total number of conducting strips, and the properties of the substrate, on the performance of a holographic antenna. This will allow us to suggest a structured design procedure for such antennas.

5.6 References for Chapter 5

[1] *LCONF* is a routine in the *IMSL Numerical Libraries*, which are products of Visual Numerics Inc., 2657 Alcosta Boulevard, Suite 450, San Ramon, CA 94583, USA.

[2] K. Lévis, A. Ittipiboon, A. Petosa, L. Roy & P. Berini, "Ka-band dipole holographic antennas', IEE Proc.-Microwave Antennas Propagation, Vol. 148, No. 2, pp.129-132, April 2001.

[3] D. Carroll, "FORTRAN Genetic Algorithm (GA) Driver", CU Aerospace, http://cuaerospace.com/carroll/ga.html

[4] Y. Rahmat-Samii & E. Michielssen (Edits.), "Electromagnetic Optimization by Genetic Algorithms" (Wiley, 1999).

[5] E. Levine, G. Malamud, S. Shtrikman & D. Treves, "A study of microstrip array antennas with the feed network", IEEE Trans. Antennas Propagat., Vol.AP-37, No.4, pp.426-433, April 1989.

CHAPTER 6

THE EFFECT OF THE NUMBER OF STRIPS AND THE SUBSTRATE PROPERTIES ON THE HOLOGRAPHIC ANTENNA PERFORMANCE

6.1 Preliminary Remarks

So far only the effect of strip width and spacing on the radiation pattern was studied. The Duroid 4003 dielectric slab with a relative permittivity of 3.38 and a thickness t of 20 mils was used for the single-sided design whose optimization was considered in this thesis. It would nevertheless be interesting to see how the antenna performance varies with the different dielectric slabs available (that is, dielectric slabs with different relative dielectric constants and thicknesses). Furthermore, the antenna whose optimization has been studied in this thesis was limited to 13 conducting strips and a substrate length of 140 mm. Thus another issue worth investigating is the effect of increasing these factors so as to create a larger version of the antenna. The above aspects are investigated in Sections 6.2 and 6.3 of this chapter using the electromagnetic simulation model.

6.2 Effect of the Dielectric Slab

The crucial role of the dielectric substrate on the holographic antenna performance has already been shown in Figures 4.2 and 4.3 of Section 4.3. Figures 6.1 to 6.4 now compare the performance with several commercially available dielectric slabs over the frequency range for the original single-sided holographic antenna. It can be seen that the dielectric slab (ε_r=3.00, t=20 mils) used in Chapter 5 is not the best choice at all

frequencies. Nevertheless the choices of dielectric substrate yielding the best antenna performance at 30 GHz are seen to be ε_r=3.00, t=20 mils; ε_r=3.38, t=20 mils; ε_r=3.48, t=20 mils; and ε_r=6.15, t=10 mils. These substrates are compared in Figure 6.5. The F lobe peak levels for these four different dielectric substrates are quite close to each other. Hence the selection of the dielectric in [1] and Chapter 5 is justified, although there are alternative options available, as shown above. Figure 6.6 shows the variation with frequency of the F lobe peak angular locations for these substrates.

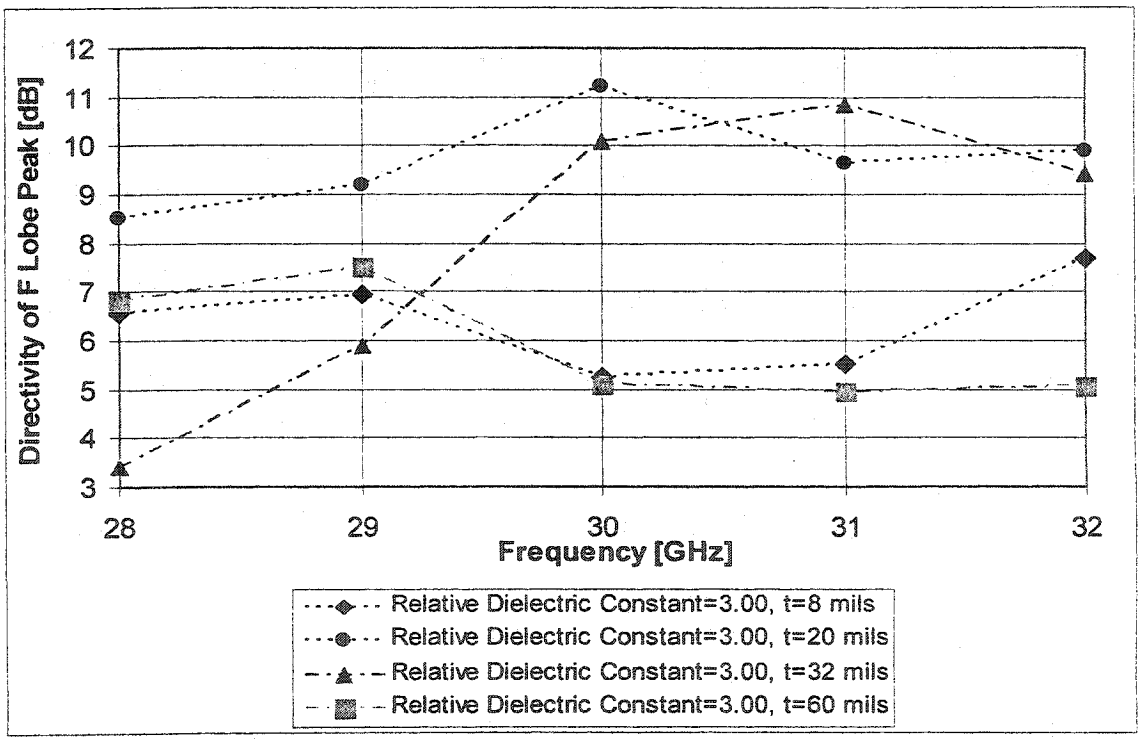

Figure 6.1: Computed F Lobe Peak Values vs. Frequency for Relative Dielectric Constant of 3.00 and Various Slab Thicknesses.

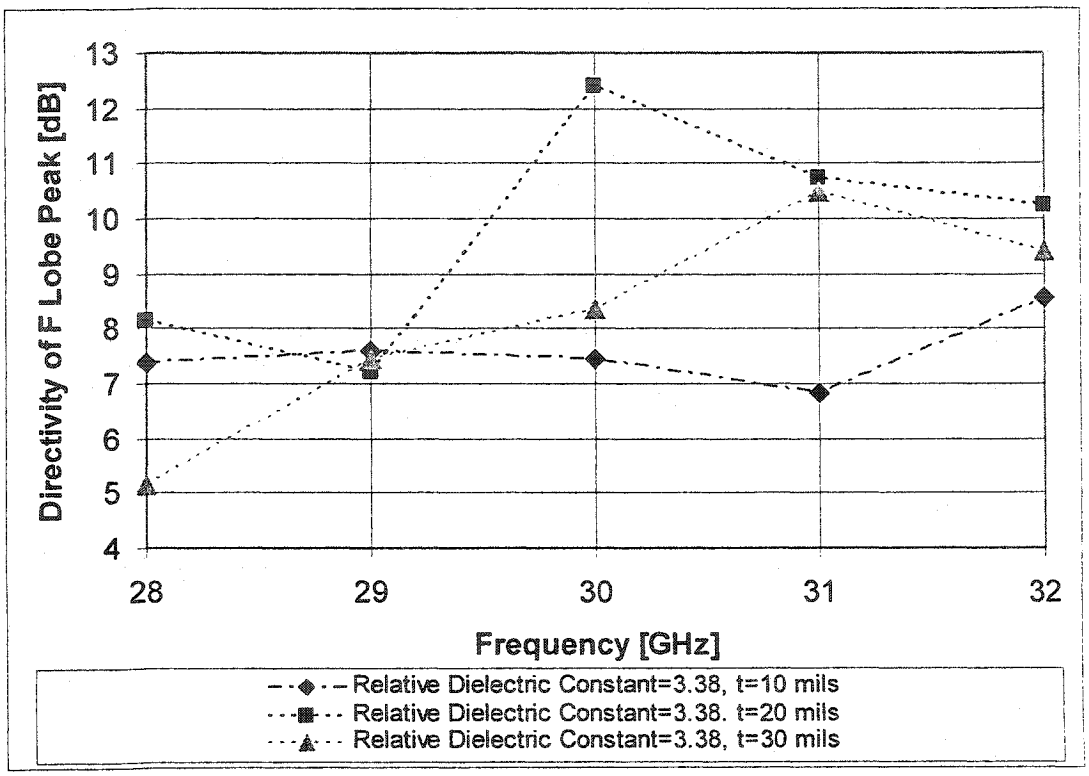

Figure 6.2: **Computed F lobe Peak Values vs. Frequency for Relative Dielectric Constant of 3.38 and Various Slab Thicknesses.**

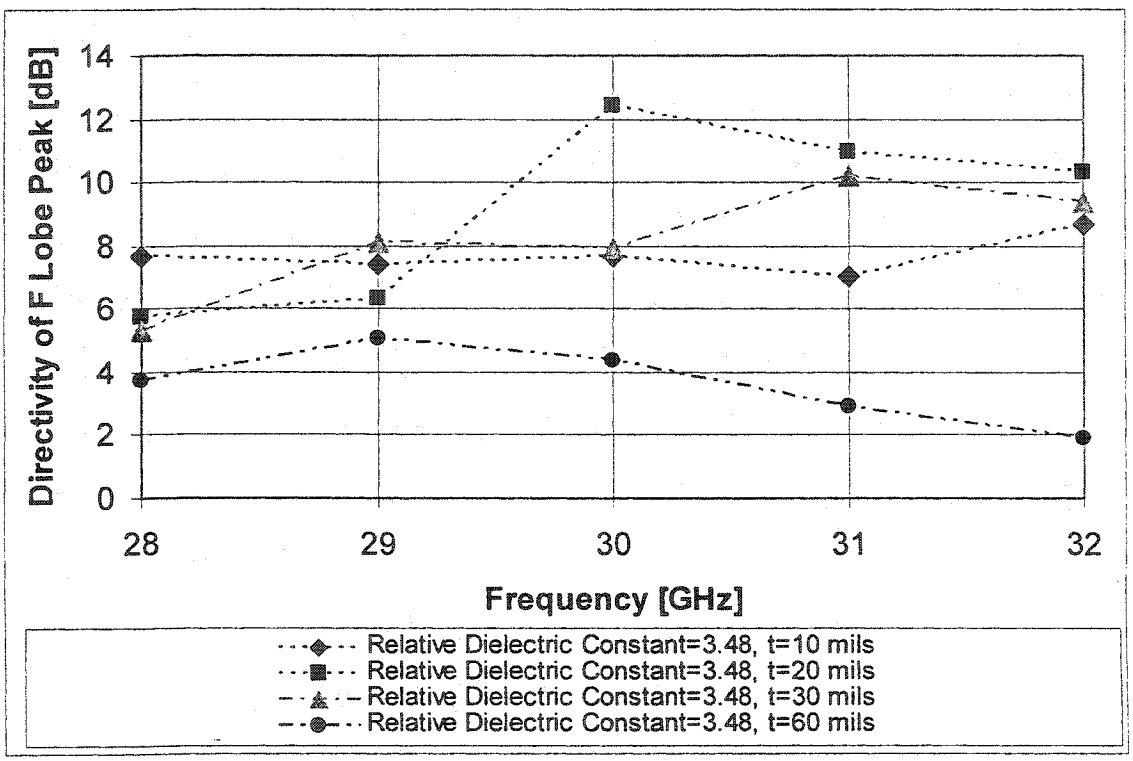

Figure 6.3: Computed F Lobe Peak Values vs. Frequency for Relative Dielectric Constant of 3.48 and Various Slab Thicknesses.

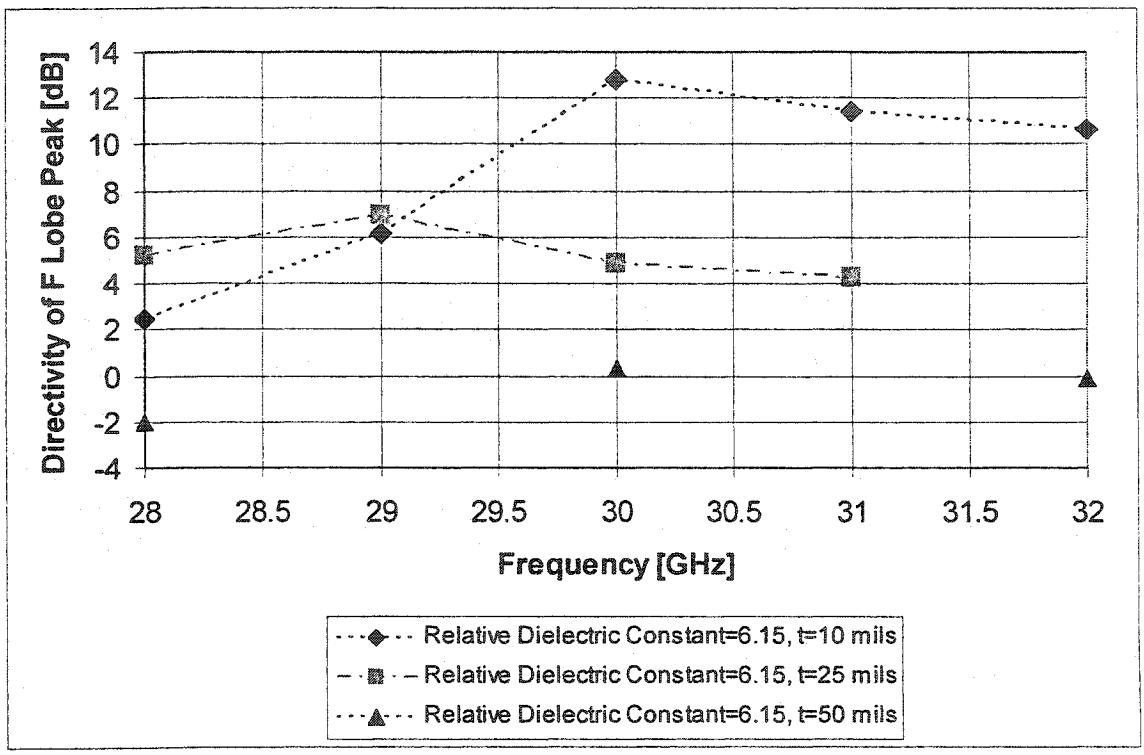

Figure 6.4: **Computed F Lobe Peak Values vs. Frequency for Relative Dielectric Constant of 6.15 and Various Slab Thicknesses.**

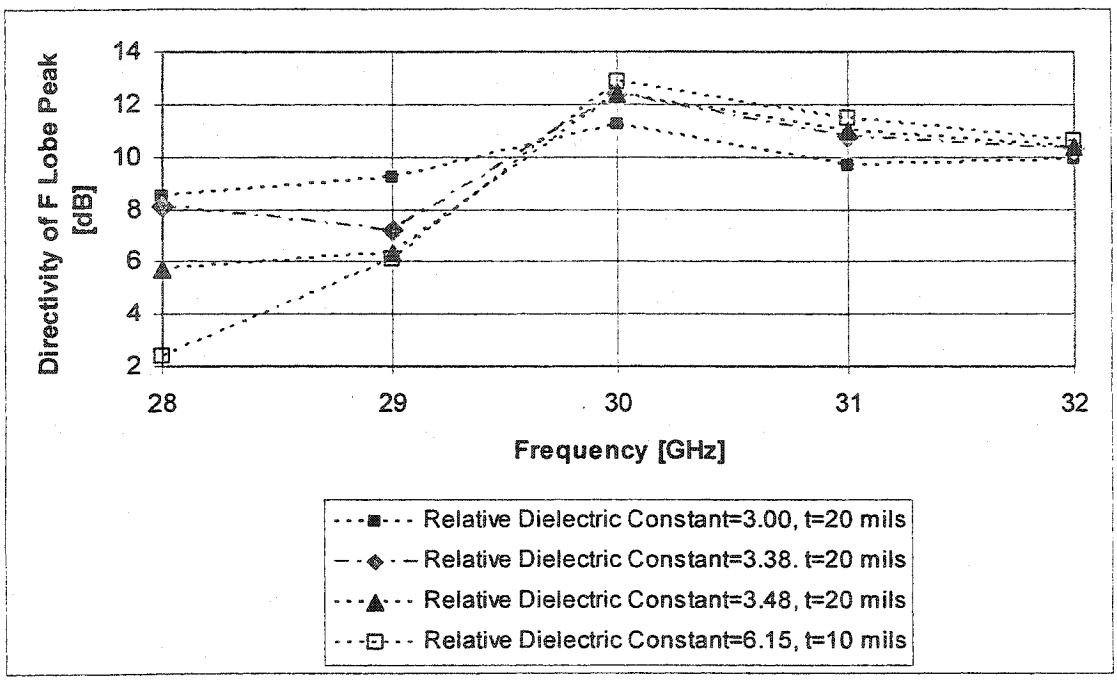

Figure 6.5: Computed F Lobe Peak Values vs. Frequency for the "Best" Values of Relative Dielectric Constant and Substrate Thicknesses.

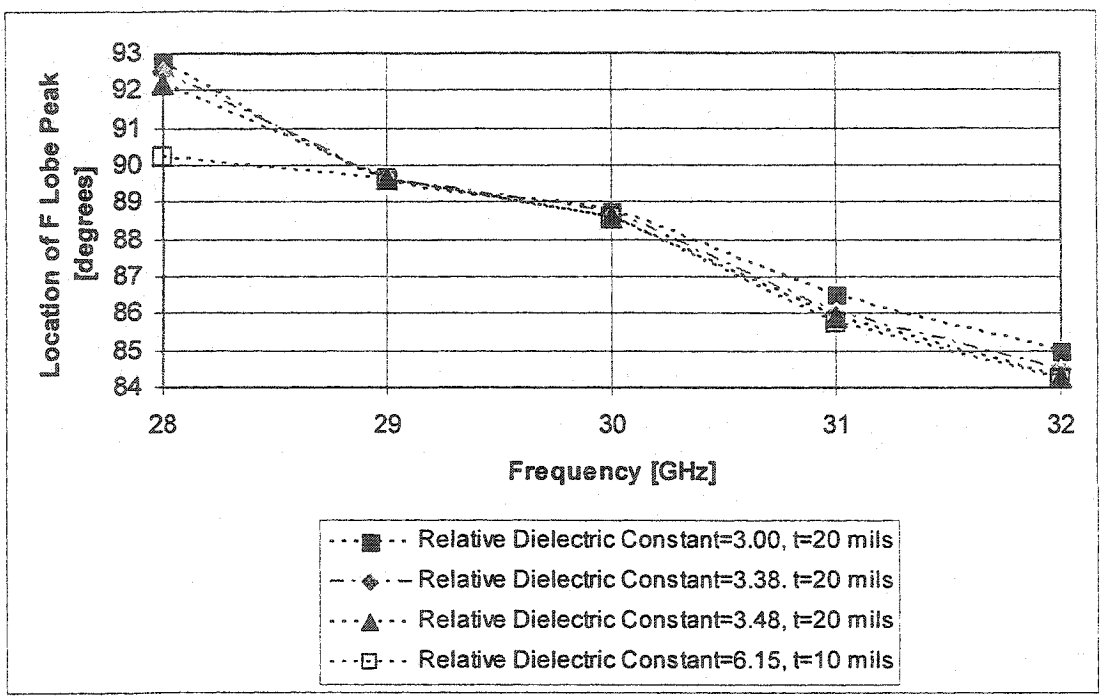

Figure 6.6: Computed F Lobe Peak Angle Location vs. Frequency for the "Best" Values of Relative Dielectric Constant and Substrate Thicknesses.

6.3 Effect of Increasing the Dielectric Slab Length and Number of Strips

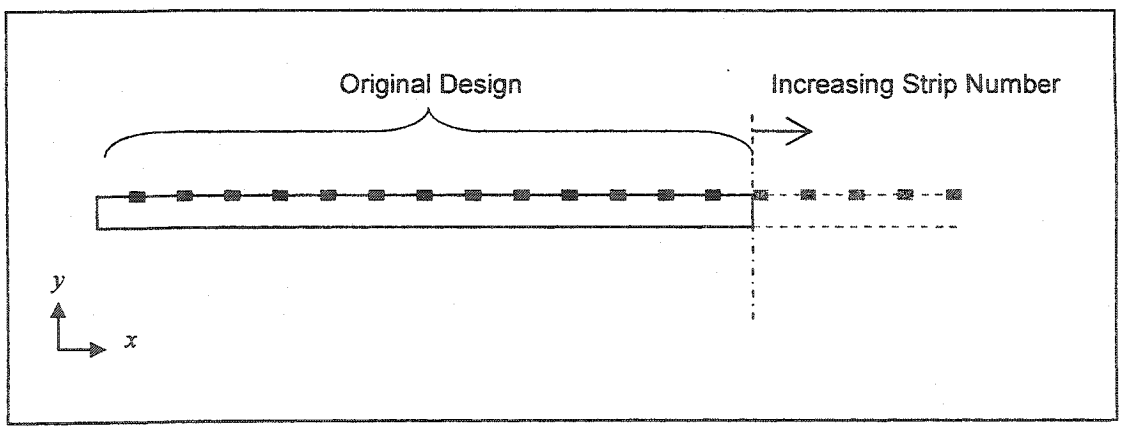

Figure 6.7: Increasing the Length and Number of Strips of the Holographic Antenna

It is possible to study the effect of increasing the length and number of strips of a holographic antenna using the electromagnetic simulation tool. The analysis is performed at 30 GHz and 26 GHz for the single and double-sided cases, respectively. Starting from

the original design of 13 strips (13 strips on each side for the double-sided design), the F lobe levels (and the B lobe in the single-sided antenna case) rise with increasing slab length and number of strips, as shown in Figures 6.8 and 6.9. It is clear that after the number of strips goes beyond a certain limit (37 strips for the cases shown) the directivity increases by a negligible amount. This sort of behaviour is intuitively expected, and is due to the fact that the E-fields travelling along the dielectric slab eventually becomes very small and the strips added are not excited by these fields beyond a certain point. This also explains why the optimized antennas in Sections 5.4.1 and 5.4.2 had larger strips towards the end of the dielectric slab furthest from the feed. The T lobe level is also seen to decrease until it too "flattens out". The electromagnetic simulation tool developed in this thesis thus provides a convenient means of determining the maximum antenna size (when fed by a horn).

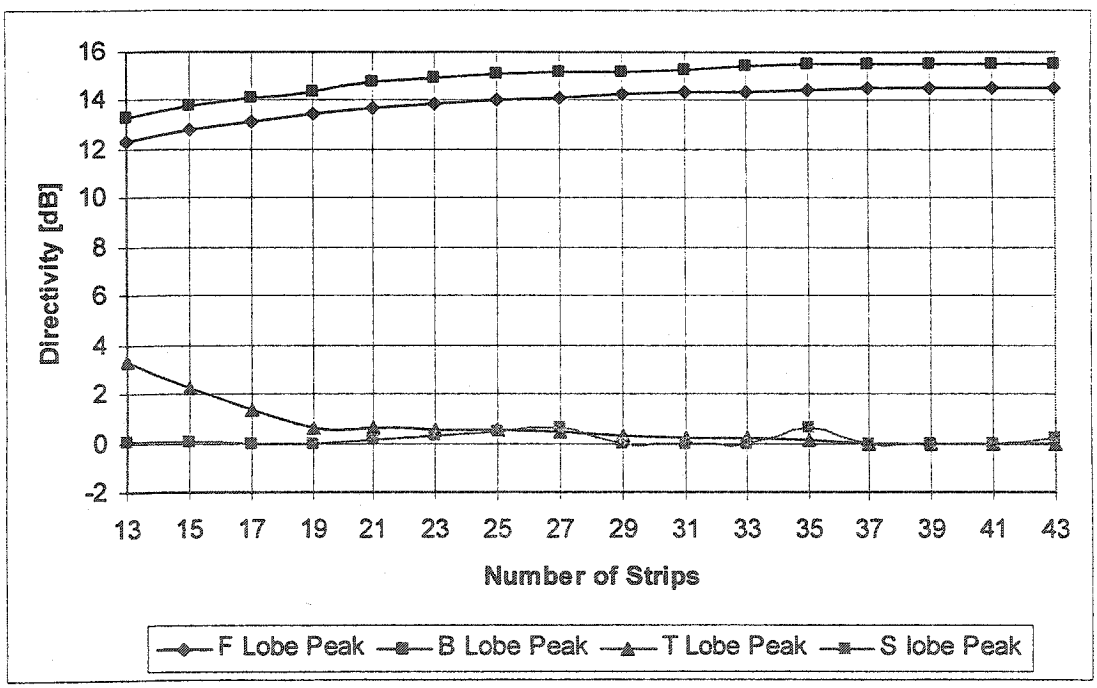

Figure 6.8: Single-Sided Antenna Performance with Increasing Number of Strips at 30 GHz

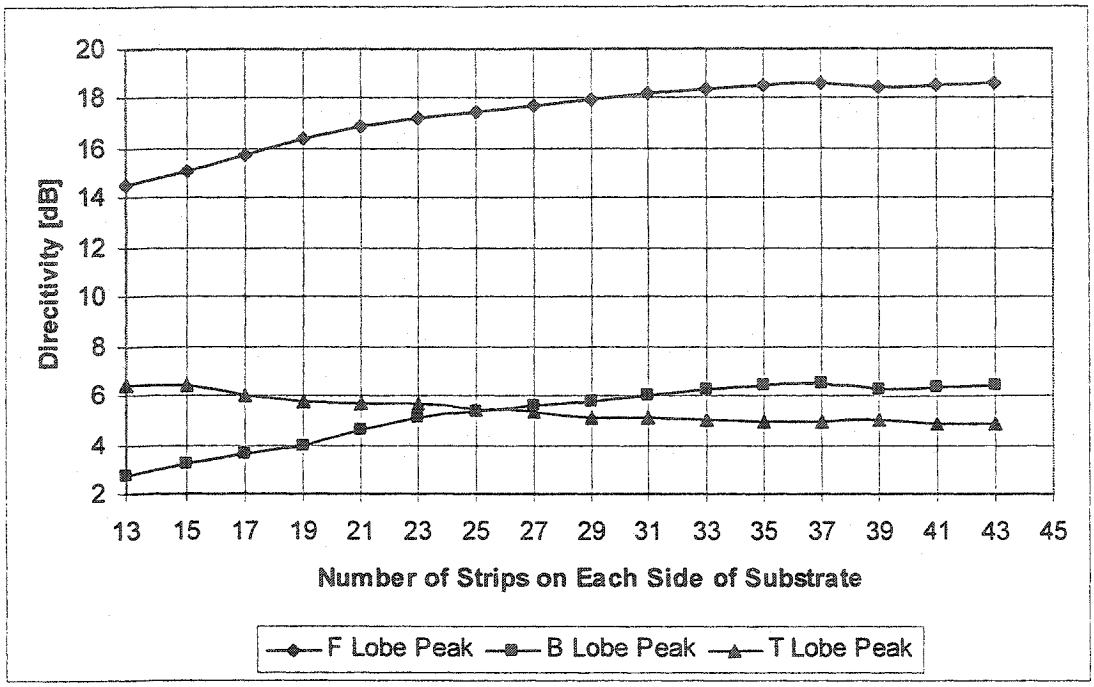

Figure 6.9: Double-Sided Antenna Performance with Increasing Number of Strips at 26 GHz

6.4 Conclusions

The dielectric constant and thickness of the slab significantly affects the performance of the antenna even for very thin substrates. Although in this thesis the dielectric substrate used had a thickness of 20 mils (60 mils) in the case of the single-sided (double-sided) antenna, and a relative permittivity of 3.38 (3.00), it has been shown in this chapter that there are other available substrates which can perform better at certain frequencies. Hence the dielectric thickness and dielectric permittivity could be used as variables in future designs in addition to strip width and spacing. However, the relative permittivities and thicknesses of substrates are not quantities that can be continuously varied under the designers' control. In practice one has to accept permittivity/thickness

combinations that are commercially available. Thus the best procedure for achieving the highest directivity might be to:

(a) Design an unoptimized holographic antenna using the methods of [1].

(b) Perform simulations for various permittivity/thickness combinations as was done in Section 6.2 to select the best substrate for the frequency band of interest.

(c) Perform simulations as in Section 6.3 to select the largest number of conducting strips worth using.

(d) Perform the optimization procedure of Chapter 5 on the resulting holographic antenna.

6.5 References for Chapter 6

[1] K. Lévis, "Ka-Band Holographic Antennas", Master of Applied Science Thesis, Faculty of Engineering, University of Ottawa, September 1999.

CHAPTER 7

General Conclusions and Future Work

The contributions of this thesis are as follows:

- A two-dimensional (2D) integral equation formulation for the problem of line-source excitation of more than one conductor/dielectric object was given. This is an extension of an existing formulation that has not previously been presented.

- A moment method formulation for the numerical solution of the above coupled integral equation model has been given, and implementable expressions given for all the resulting matrix equation elements.

- The validity of the coupled integral equation 2D electromagnetic model as a means of modeling a planar holographic antenna's pattern performance in its H-plane was demonstrated experimentally. This has not been done elsewhere.

- The 2D electromagnetic model was coupled to a numerical optimization procedure in order to arrive at holographic antennas (of a specified number of conducting strips) with maximized directivity. The computational feasibility of the approach was demonstrated, and its suitability is shown through measurements performed on antennas optimized in this way. It is believed that this is the first time such an approach has been implemented and described for this class of antennas.

- The 2D electromagnetic model was used to examine the effect of factors such as the substrate relative permittivity and thickness.

- A structured design procedure has been suggested for the class of holographic antennas studied.

Future work might include the following:

- The structured design procedure suggested could be applied in order to realize holographic antennas with the highest possible directivity.

- The electromagnetic simulation tool could be applied to design a holographic antenna whose hologram is realized entirely using dielectric material.

- The electromagnetic model developed in this thesis could be used to compute the near-zone fields on the holographic antenna and from this the propagation constants of the waves traveling along the substrate. This might enable one to obtain further insight into the antenna operation.

APPENDIX A

Coordinate Systems

The surface of the horn, dielectric and strips can be approximated by straight line segments. The j^{th} segment connects points $t_1(j)$ and $t_2(j)$ as shown in Figure A.1.

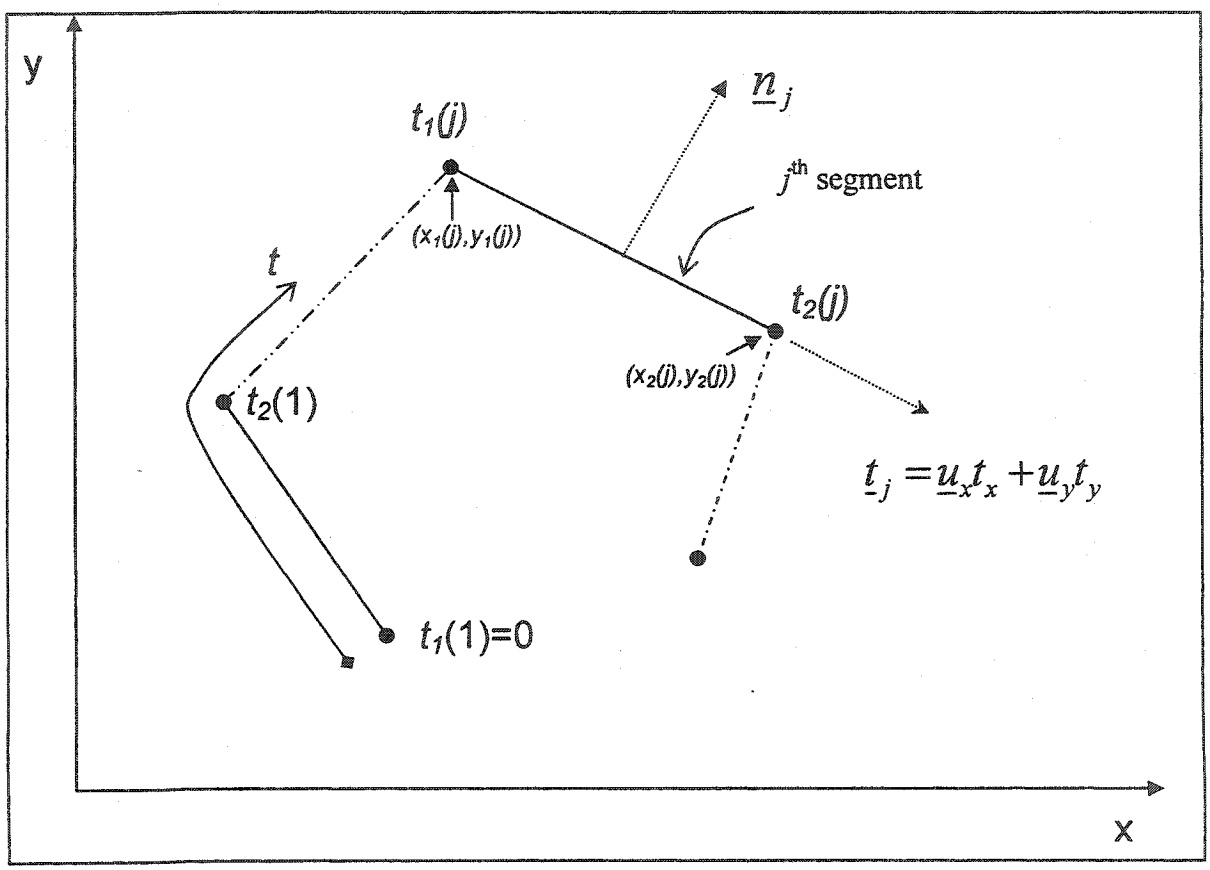

Figure A.1: Vector Coordinate System

Quantity t is the arc length along the contour starting from $t_1(1)$. The unit vector tangential to the j^{th} segment can be written as

$$\underline{t}_j = \frac{\underline{u}_x\{x_2(j)-x_1(j)\}+\underline{u}_y\{y_2(j)-y_1(j)\}}{\Delta C_j} \qquad \text{(A-1)}$$

with

$$\Delta C_j = \sqrt{[x_2(j) - x_1(j)]^2 + [y_2(j) - y_1(j)]^2} \tag{A-2}$$

Hence the normal to the j^{th} segment can be obtained from vector cross-multiplication shown in (A-3) and this result is used in deriving (3-31a) from (3-30).

$$\underline{n}_j = \underline{z} \times \underline{t}_j = \begin{vmatrix} \underline{u}_x & \underline{u}_y & \underline{u}_z \\ 0 & 0 & 1 \\ t_x & t_y & 0 \end{vmatrix} = -\underline{u}_x t_y + \underline{u}_y t_x \tag{A-3}$$

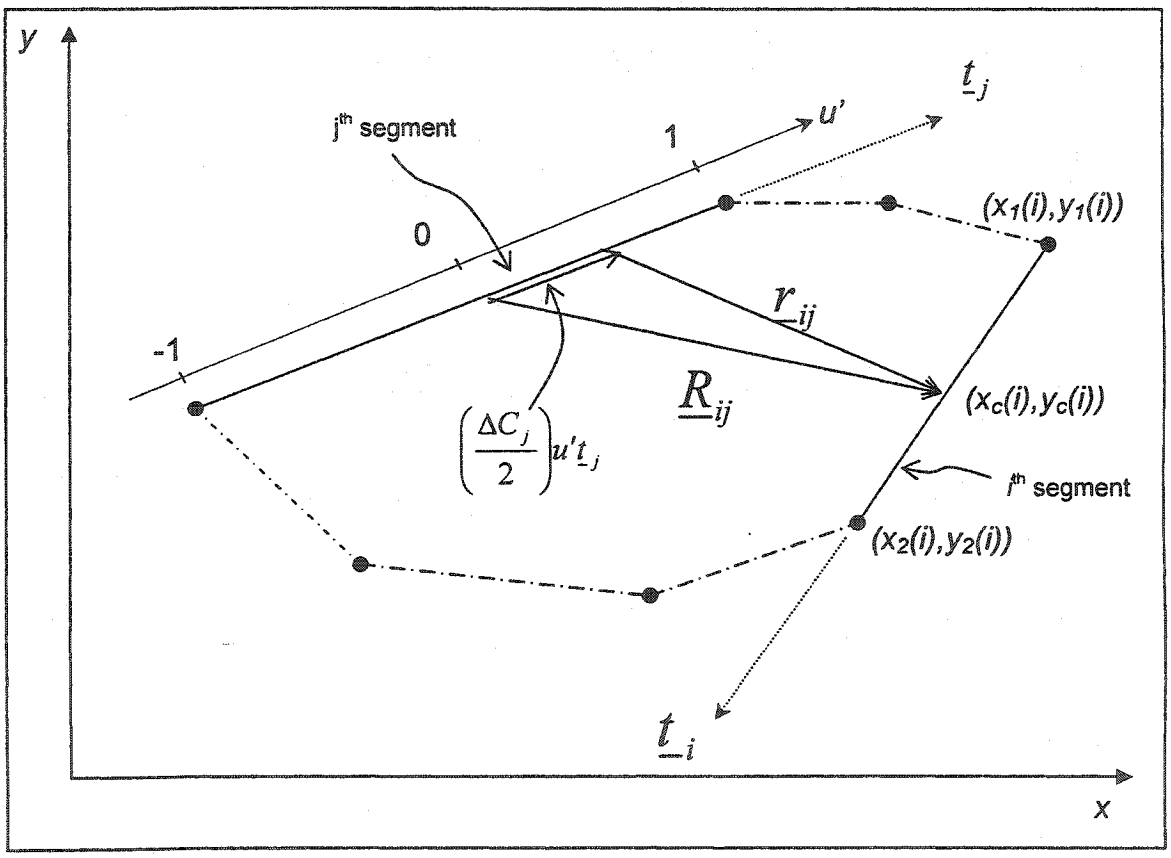

Figure A.2: Vector Coordinate System Showing Inter-Segment Vectors and Distances

From Figure A.2, the following equalities can be obtained

$$\left(\frac{\Delta C_j}{2}\right)u'\underline{t}_j + \underline{r}_{ij} = \underline{R}_{ij} \quad \Rightarrow \quad \underline{r}_{ij} = \underline{R}_{ij} - \left(\frac{\Delta C_j}{2}\right)u'\underline{t}_j \tag{A-4}$$

$$\underline{R}_{ij} = \underline{u}_x\left(x_c(j) - x_c(i)\right) + \underline{u}_y\left(y_c(j) - y_c(i)\right) \tag{A-5}$$

$$\left(\frac{\Delta C_j}{2}\right)\underline{t}_j = \frac{1}{2}\underline{u}_x\left\{x_2(j) - x_1(j)\right\} + \frac{1}{2}\underline{u}_y\left\{y_2(j) - y_1(j)\right\} \tag{A-6}$$

(A-5) and (A-6) into (A-4) results in

$$\underline{r}_{ij} = \underline{u}_x\left\{x_c(j) - x_c(i) - \frac{u'}{2}\left[x_2(j) - x_1(j)\right]\right\} + \underline{u}_y\left\{y_c(j) - y_c(i) - \frac{u'}{2}\left[y_2(j) - y_1(j)\right]\right\} \tag{A-7}$$

and thus

$$r_{ij} = \left|\underline{r}_{ij}\right| = \sqrt{a_x^2 + a_y^2} \tag{A-8a}$$

where

$$a_x = x_c(j) - x_c(i) - \frac{u'}{2}\left[x_2(j) - x_1(j)\right] \tag{A-8b}$$

$$a_y = y_c(j) - y_c(i) - \frac{u'}{2}\left[y_2(j) - y_1(j)\right] \tag{A-8c}$$

The expressions defined in this Appendix are used to evaluate the expressions (3-36a) through (3-40c).

APPENDIX B

Electric and Magnetic Fields Due to an Infinitely Long Electric Line Source

The electric field, at the observation point (x,y) in free-space, due to an infinitely long line source at (x_o,y_o) is known to be [1]

$$\hat{E}_z^i(x,y) = -\frac{\kappa_o^2}{4\omega\varepsilon_o} H_0^{(2)}\left(\kappa_o\sqrt{(x-x_o)^2+(y-y_o)^2}\right) \tag{B-1}$$

The magnetic field can be obtained from by using the Maxwell equation

$$\underline{\hat{H}}^i(x,y,z) = -\frac{1}{j\omega\mu_o}\underline{\nabla}\times\underline{\hat{E}}^i(x,y,z) \tag{B-2}$$

Knowing that the E-field has a z-component only, and performing the vector algebra, (B-2) yields

$$\underline{\hat{H}}^i(x,y) = -\frac{1}{j\omega\mu_o}\left\{\hat{x}\frac{\partial\hat{E}_z^i(x,y)}{\partial y} - \hat{y}\frac{\partial\hat{E}_z^i(x,y)}{\partial x}\right\} \tag{B-3}$$

We can separate the H-field components as follows:

$$\hat{H}_x^i(x,y) = -\frac{1}{j\omega\mu_o}\frac{\partial\hat{E}_z^i(x,y)}{\partial y} \tag{B-4}$$

$$\hat{H}_y^i(x,y) = \frac{1}{j\omega\mu_o}\frac{\partial\hat{E}_z^i(x,y)}{\partial x} \tag{B-5}$$

Substituting (B-1) into (B-4) and (B-5), and differentiating, we obtain

$$\hat{H}_x^i(x,y) = -\frac{\kappa_o^2}{4j}(y-y_o)\frac{H_1^{(2)}\left\{\kappa_o\sqrt{(x-x_o)^2+(y-y_o)^2}\right\}}{\kappa_o\sqrt{(x-x_o)^2+(y-y_o)^2}} \tag{B-6}$$

$$\hat{H}_y^i(x,y) = \frac{\kappa_o^2}{4j}(x-x_o)\frac{H_1^{(2)}\left\{\kappa_o\sqrt{(x-x_o)^2+(y-y_o)^2}\right\}}{\kappa_o\sqrt{(x-x_o)^2+(y-y_o)^2}} \tag{B-7}$$

References for Appendix B

[1] R.F. Harrington, "Time-Harmonic Electromagnetic Fields" (McGraw-Hill, 1961) pp.223-228

APPENDIX C

The Two-Dimensional Directivity

The two-dimensional directivity can be calculated in a manner similar to the three-dimensional case. The directivity at an angle ϕ is the ratio of the radiation intensity at that angle to the average radiation intensity over the interval 0 to 2π. Thus we have

$$D(\phi) = \frac{U(\phi)}{U_{avg}} \tag{C-1}$$

For this 2-D case, the radiation intensity can be related to the power density $S(\phi)$ by

$$U(\phi) = \rho S(\phi) \tag{C-2}$$

where ρ is defined in Section 3.3. The Power density can be written in terms of the electric field as

$$S(\phi) = \frac{|E_z(\rho,\phi)|^2}{2\eta_o} \tag{C-3}$$

The two dimensional electric field in the far-zone takes the form

$$E_z(\rho,\phi) \rightarrow \frac{e^{-jk\rho}}{\sqrt{\rho}} E_z(\phi) \tag{C-4}$$

Expressions (C-3) and (C-4) into (C-2) gives

$$U(\phi) = \frac{|E_z(\phi)|^2}{2\eta_o} \tag{C-5}$$

Finally (C-5) into (C-1) gives

$$D(\phi) = \frac{|E_z(\phi)|^2}{\frac{1}{2\pi}\int_0^{2\pi} |E_z(\phi)|^2 \, d\phi} \tag{C-6}$$

APPENDIX D

Holographic Antenna Dimensions

D.1 Single-Sided Holographic Antenna

Table D.1: Single-Sided Holographic Antenna Dimensions

Dielectric Thickness (mils)	20.00
Dielectric Length (mm)	140.00
Dielectric Relative Permittivity	3.38
Feed Point (mm)	0.00

Table D.2: Original Single-Sided Holographic Antenna Strip Dimensions

Strip Number	Strip Width (mm)	Strip Center Displacement from Left Edge of Dielectric (mm)
1	0.254	10.00
2	0.254	20.00
3	0.254	30.00
4	0.254	40.00
5	0.254	50.00
6	0.254	60.00
7	0.254	70.00
8	0.254	80.00
9	0.254	90.00
10	0.254	100.00
11	0.254	110.00
12	0.254	120.00
13	0.254	130.00

Table D.3: Optimized Single-Sided Holographic Antenna Strip Dimensions

Strip Number	Strip Width (mm)	Strip Center Displacement from Left Edge of Dielectric (mm)
1	0.2545	10.4639
2	0.254	19.6561
3	0.2899	29.5325
4	0.3186	39.2403
5	0.254	47.9136
6	0.3182	56.6493
7	0.8472	70.0268
8	0.6381	79.3357
9	0.7821	88.8225
10	1.3827	98.582
11	1.4147	108.3511
12	2.0236	118.3698
13	0.8393	128.1654

D.2 Double Sided Holographic Antenna

Table D.4: Double-Sided Holographic Antenna Dimensions

Dielectric Thickness (mils)	60.00
Dielectric Length (mm)	140.00
Dielectric Relative Permittivity	3.00
Feed Point (mm)	0.00

Table D.5: Original Double-Sided Holographic Antenna Strip Dimensions

Strips on the Top Side of the Slab		
Strip Number	Strip Width (mm)	Strip Center Displacement from Left Edge of Dielectric (mm)
1	0.254	10.00
2	0.254	20.00
3	0.254	30.00
4	0.254	40.00
5	0.254	50.00
6	0.254	60.00
7	0.254	70.00
8	0.254	80.00
9	0.254	90.00
10	0.254	100.00
11	0.254	110.00
12	0.254	120.00
13	0.254	130.00
Strips on the Bottom Side of the Slab		
1	0.254	7.5
2	0.254	17.5
3	0.254	27.5
4	0.254	37.5
5	0.254	47.5
6	0.254	57.5
7	0.254	67.5
8	0.254	77.5
9	0.254	87.5
10	0.254	97.5
11	0.254	107.5
12	0.254	117.5
13	0.254	127.5

Table D.6: Optimized Double-Sided Holographic Antenna Strip Dimensions

Strips on the Top Side of the Slab		
Strip Number	Strip Width (mm)	Strip Center Displacement from Left Edge of Dielectric (mm)
1	0.303811	7.363971
2	1.140791	17.02252
3	0.561886	27.12738
4	0.532648	37.24788
5	0.258277	47.68069
6	0.254	58.19383
7	0.254	68.92103
8	0.254	79.55039
9	0.269061	89.76368
10	0.829826	100.2966
11	0.396219	110.9988
12	0.582234	121.8186
13	0.772413	132.7565
Strips on the Bottom Side of the Slab		
1	0.501804	6.813606
2	0.2632	13.12411
3	0.254	25.51677
4	0.254	35.35467
5	0.261666	45.37395
6	0.254	55.48583
7	0.455888	65.9416
8	0.532436	76.29404
9	0.365942	86.48094
10	0.441007	97.45245
11	0.700332	108.3876
12	1.460415	119.3578
13	1.357778	130.052

APPENDIX E

Antenna Measurement Setup and the Sectoral Feed Horn

E.1 H-Plane Sectoral Horn Antenna

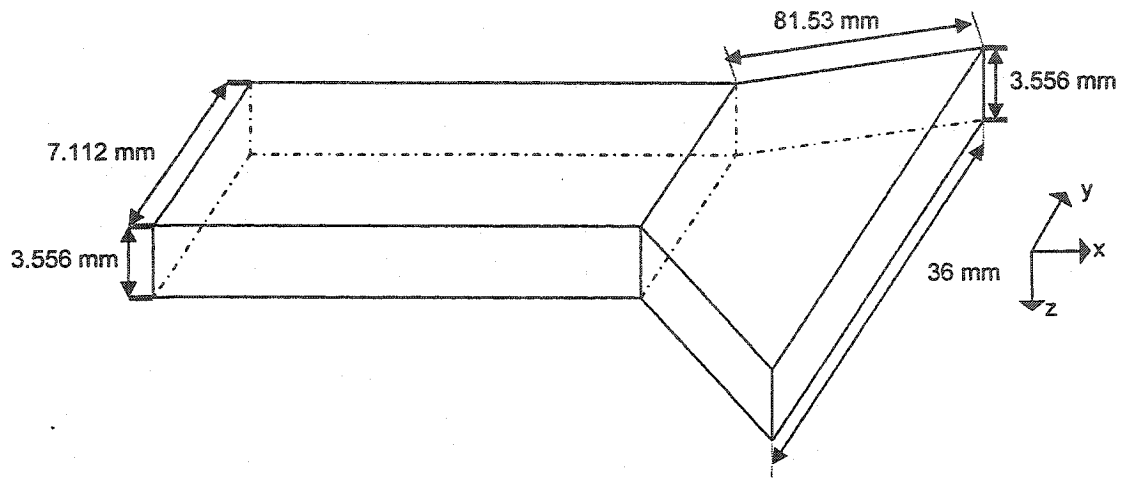

Figure E.1: Dimensions of the H-plane Sectoral Horn Antenna

The 3-D view of the H-plane sectoral horn antenna, used as the feed for the holographic antenna, is shown above in Figure E.1. Only the x-y plane (H-plane) of the horn antenna is of interest when performing 2-D simulations. Figure E.2 shows the measured H-plane radiation pattern of the horn antenna at 26 GHz, from which the beamwidth is measured to be approximately 20 degrees. The maximum gain, and beamwidth in the H-plane, over the frequency range 24 to 30 GHz is given in Table E.1 below.

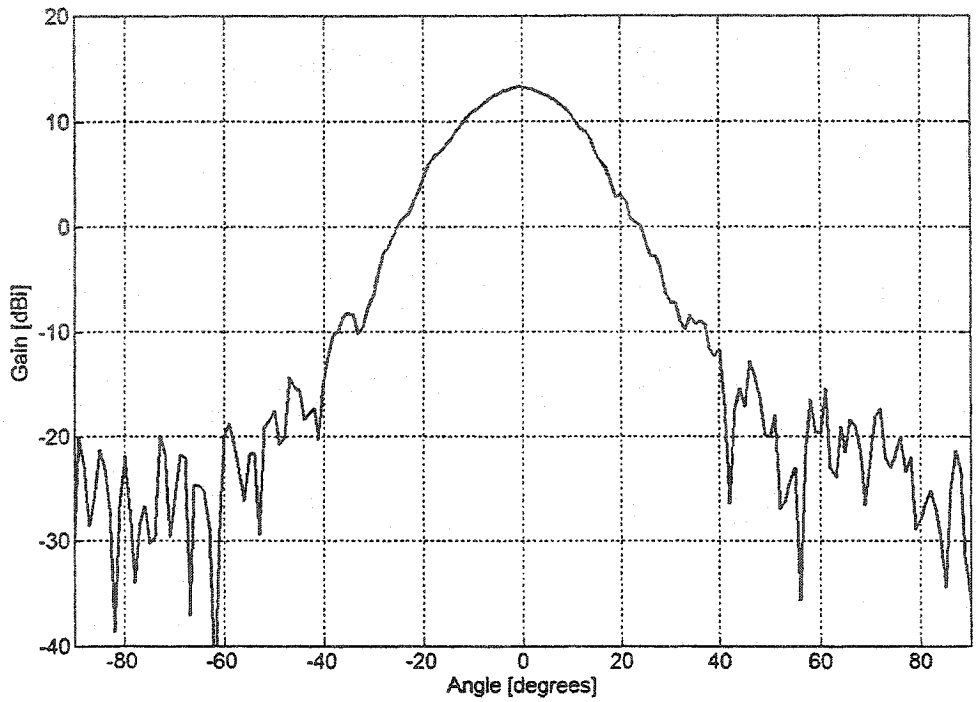

Figure E.2: **Measured H-Plane Radiation Pattern of the Feed Horn Antenna at 26 GHz**

Table E.1: **Measured H-plane Radiation Pattern Characteristics of the Feed Horn Antenna with Frequency**

Frequency [GHz]	Maximum Gain [dBi]	3-dB Beamwidth [degrees]
24	13.20	23.1
25	12.40	20.3
26	13.30	21.7
27	13.20	18.5
28	13.50	20.0
29	13.72	19.2
30	13.80	18.7

E.2 Holographic Antenna Pattern Measurement Test-Jig

The setup is shown in Figure E.3 below. The hologram is supported by two anti-reflective carbon rods. The H-plane radiation pattern of this setup is shown in Figure E.4 below. The test-jig was devised by Mr. David Lee of the Advanced Antenna Technology Lab Group of the Communications Research Centre.

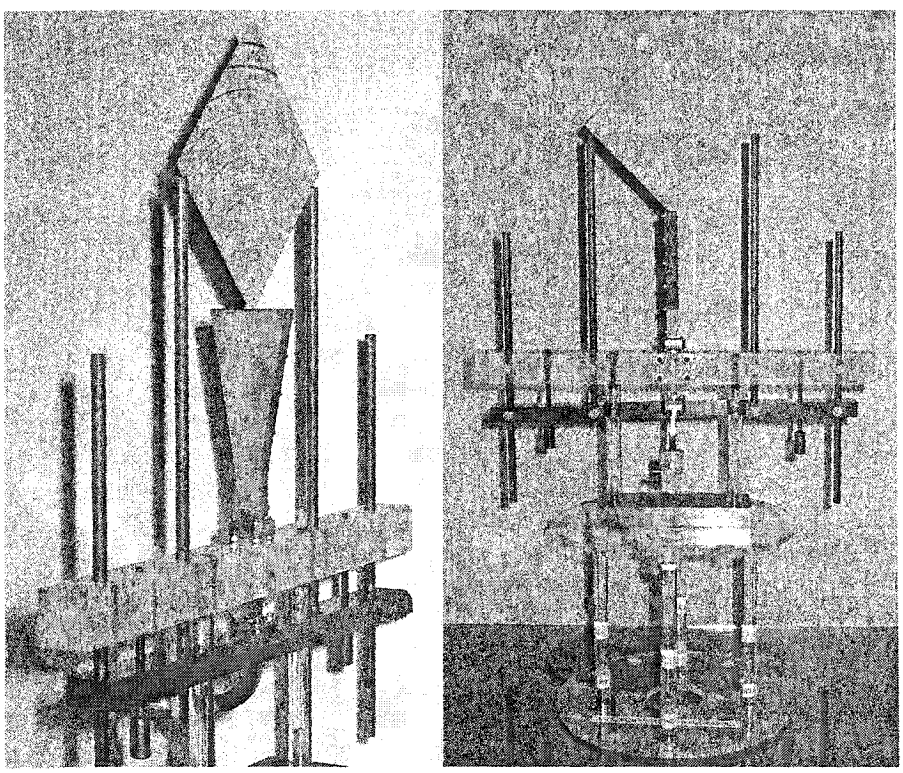

Figure E.3: Holographic Antenna Measurement Setup

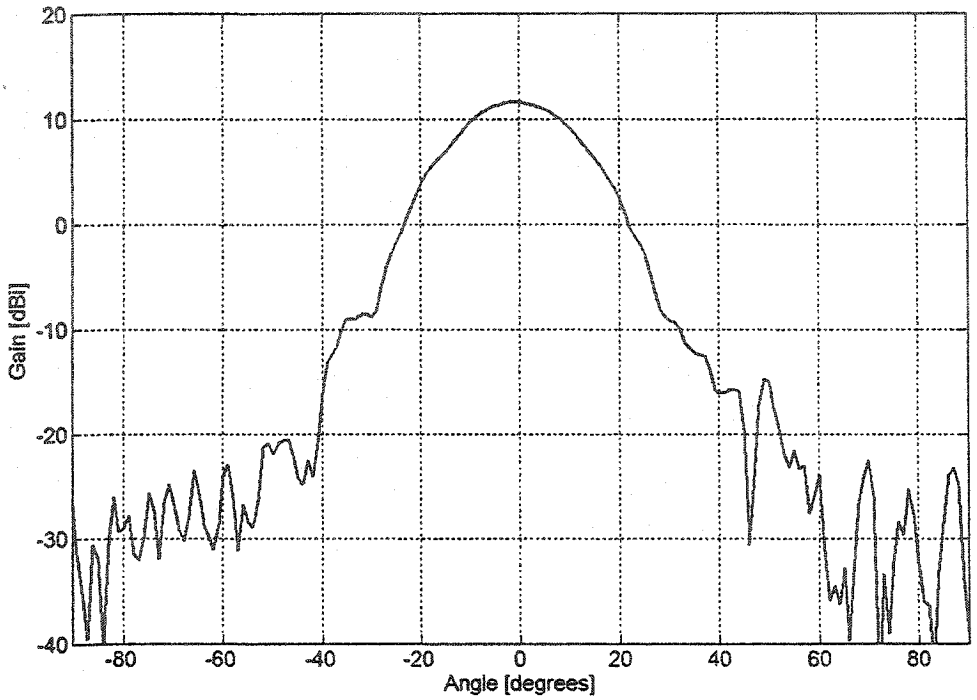

Figure E.4: Measured H-Plane Radiation Pattern of the Horn Antenna with the Measurement Setup at 26 GHz